Chapter 4

Development of diverse (5,5)CC transient compact schemes for computation of fluid flow and heat transfer on nonuniform polar grids

4.1 Introduction

Fluid flow problems involving circular geometries have attracted a significant amount of attention over the years due to their theoretical significance and physical relevance. For such importance, HOC schemes have been developed in the cylindrical polar coordinates because of their potential in delivering higher accuracy with lower computational cost. Preliminary works to develop HOC schemes in the cylindrical polar coordinate system mostly focused on the Poisson equation and uniform grids [9, 67, 68, 88, 89, 187]. Here, it is important to mention that in polar coordinates Poisson equation involves variable coefficients and thus the above-mentioned works involved significant endeavors and were not mere extension of the works done in the Cartesian coordinates. Additionally, a valid discretization at singularity $r = 0$ is necessary. Subsequently, considerable efforts could be found in the literature on HOC discretization of N-S equations in the body-fitted polar coordinate system [26, 69, 123, 126, 176]. In the year 2005, Sanyasiraju and Manjula [126] proposed a higher-order semicompact technique to solve the flow around an impulsively started

circular cylinder. The authors used a wider stencil to discretize a few terms of the governing equation rendering semicompactness to the scheme. This strategy also helped alleviate challenges associated with the variable coefficients of the second-order derivative. Subsequently, Kalita and Ray [69] developed a spatially third-order and temporally second-order accurate higher-order compact scheme for $\psi-\omega$ formulation of unsteady N-S equations. As the authors worked with a modified differential equation, the resulting difference equation carried a higher order of singularity. The scheme was specially adapted to simulate incompressible flow past a circular cylinder directly on nonuniform polar grids. A rather straightforward adaptation of this scheme for steady convection-diffusion equation (CDE) can be found in [123]. In the year 2013, the pioneering work on compact difference schemes for the pure streamfunction formulation of N-S equations in polar coordinates was reported by Yu and Tian [176]. The authors here worked with the steady biharmonic equation in polar coordinates. The scheme developed therein is of second-order accuracy and carries streamfunction and its first-order derivatives as the unknown variables. Of late, Das *et al.* [26] also worked with steady second-order equation with variable coefficients in polar coordinates and introduced a third-order accurate HOC scheme. The scheme claimed to be implemented on a nonuniform grid used an implicit form of first-order derivatives and was successful in simulating steady incompressible flows. It is clear from the above discussion that classical HOC discretization of transient generalized second-order PDE with variable coefficients in polar coordinates has not been attempted apart from the work of Kalita and Ray [69] on streamfunction-vorticity form of the N-S equations, whose extension to other governing equations such as the Boussinesq equations is not immediate. Additionally, it is intriguing to notice that developed HOC schemes in polar coordinates have been traditionally used to handle the nonuniformity of grids in radial direction only. However, heat and fluid flow problems are often associated with generation of steep gradients of streamfunction and vorticity near the bluff body or domain boundary walls and as such, grid clustering in all directions should be economical.

Here, we intend to work with new transient compact formulations which can solve fluid flow as well as heat transfer problems directly in polar coordinates. Schemes

conceived in the process must be generalizable to approximate second-order equations with variable coefficients in polar coordinates and should be efficient for circular geometries. Starting with a second-order PDE with variable coefficients, we advocate a spatially second-order accurate discretization strategy amenable for extension to a nonlinear system of N-S equations and beyond. Subsequently, this strategy is manipulated further to introduce a new HOC scheme which carries third-order convergence. Additionally, we adopt the philosophy of nonuniform grids for accurate resolution of complex flow problems. We look forward to combining the virtues of compact approximation of second-order derivatives in terms of flow variables and their first-order gradients and Padé approximation of first-order derivatives on nonuniform grids with variable coefficients. The schemes developed here lead to stable higher-order discretization in case of both Dirichlet and convective boundary conditions. The formulations are validated by applying it to the N-S equations and the problem of an unsteady Gaussian pulse governed by the linear CDE. Both these problems are equipped with known analytical solutions, which helps in error analysis as well. Besides, we are also concerned to carry out a comparison study between the solutions computed using newly proposed second-order and third-order compact schemes. The spatial and temporal order of convergences are also established during this process. However, to comprehend the robustness and adaptability of the new schemes, we carry out the simulations for benchmark problems of both flow and heat transfer, namely the flow inside a driven polar cavity, natural convection inside a circular annulus, and forced convection around a stationary circular cylinder. These flows are governed by N-S equations and Boussinesq equations, both the equations being cast in transient incompressible form. The $\psi - \omega$ formulation of these coupled nonlinear systems are tackled in the present computation.

The rest of the chapter is organised in four sections. In section 4.2, compact discretization of transient CDE on cylindrical polar coordinate grids is shown. The solution technique of algebraic system of equations is discussed in section 4.3. The five test cases are described in the section 4.4 and finally, section 4.5 gives a gist of the study.

4.2 Mathematical formulation and discretization procedure

The discretization process closely resembles that which is described in Chapter 3. In the nonrectangular domain $\Omega = [a_r, b_r] \times [a_\theta, b_\theta]$, the polar (r, θ) form of the CDE (3.2) is

$$a\phi_t - \phi_{rr} - \frac{1}{r^2}\phi_{\theta\theta} + \mathscr{c}_1(r,\theta,t)\phi_r + \mathscr{c}_2(r,\theta,t)\phi_\theta = f(r,\theta,t), \tag{4.1}$$

with convection coefficients $\mathscr{c}_1$ and $\mathscr{c}_2$ as

$$\mathscr{c}_1(r,\theta,t) = c_1(x,y,t)\cos\theta + c_2(x,y,t)\sin\theta - \frac{1}{r},$$

and

$$\mathscr{c}_2(r,\theta,t) = \frac{1}{r}\left(-c_1(x,y,t)\sin\theta + c_2(x,y,t)\cos\theta\right)$$

respectively.

Both the coefficients carry singularity at $r = 0$ and as such, require special treatments at the origin. Same, being problem dependent, will be discussed in appropriate subsections.

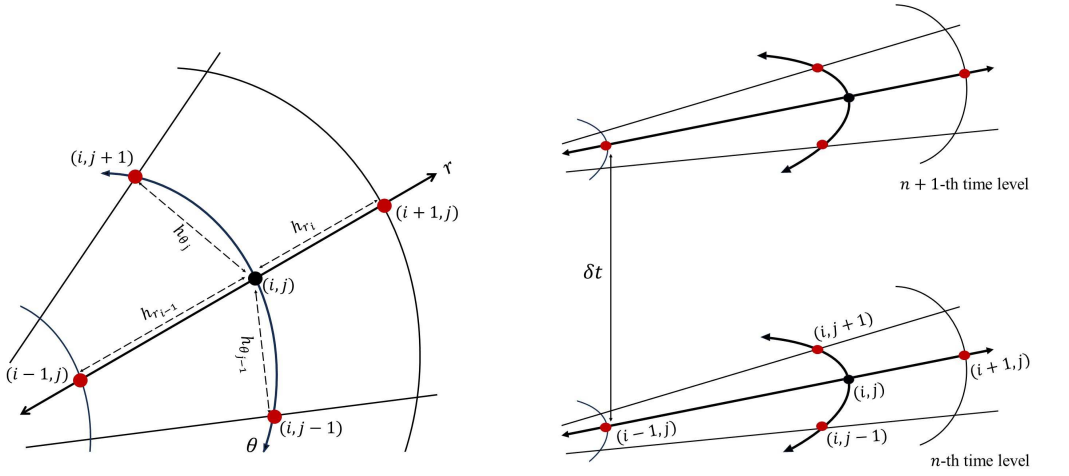

(a) (b)

Fig. 4.1: (a) Projection of nonuniform computational stencil in (r, θ) plane and (b) Nonuniform computational stencil in (r, θ, t) hyper-plane.

We discretize the domain by considering $a_r = r_1 < r_2 < r_3 < \cdots < r_{n_r} = b_r$ and $a_\theta = \theta_1 < \theta_2 < \theta_3 < \cdots < \theta_{n_\theta} = b_\theta$ where lengths between two consecutive r_i's, $i \in \{1, 2, 3, \ldots, n_r\}$ and θ_j's, $j \in \{1, 2, 3, \ldots, n_\theta\}$ may be unequal. A typical stencil can be seen in Fig. 4.1. The figure depicts the grid points at the nth and $(n+1)$th time level as well. We define the mesh sizes along radial and tangential directions to be

$$h_{r_i} = r_{i+1} - r_i, \quad i \in \{1, 2, 3, \ldots, n_r - 1\},$$
$$h_{\theta_j} = \theta_{j+1} - \theta_j, \quad j \in \{1, 2, 3, \ldots, n_\theta - 1\}.$$

For the sufficiently smooth transport variable $\phi(r, \theta)$, the finite difference operators δ_r and δ_r^2 in the radial direction are defined as

$$\delta_r \phi_{i,j} = \frac{1}{h_i + h_{i-1}} \left(\phi_{i+1,j} - \phi_{i-1,j}\right), \tag{4.2}$$

and

$$\delta_r^2 \phi_{i,j} = \frac{2}{h_{r_i} + h_{r_{i-1}}} \left[\frac{\phi_{i+1,j}}{h_{r_i}} + \frac{\phi_{i-1,j}}{h_{r_{i-1}}} - \left(\frac{1}{h_{r_i}} + \frac{1}{h_{r_{i-1}}}\right) \phi_{i,j}\right] \tag{4.3}$$

respectively, where $\phi_{i,j}$ denotes $\phi(r_i, \theta_j)$.

Considering the transport variable $\phi(r, \theta)$ to be sufficiently smooth, the first-order partial derivative $\partial_r \phi$ and second-order partial derivative $\partial_{rr} \phi$ along the r-direction at a point (r_i, θ_j) can be expressed as

$$\begin{aligned} \partial_r \phi_{i,j} = \delta_r \phi_{i,j} - \frac{1}{2}\left(h_{r_i} - h_{r_{i-1}}\right) \partial_{rr} \phi_{i,j} - \frac{1}{6}\left(\frac{h_{r_i}^3 + h_{r_{i-1}}^3}{h_{r_i} + h_{r_{i-1}}}\right) \partial_{rrr} \phi_{i,j} \\ - \frac{1}{24}\left(\frac{h_{r_i}^4 - h_{r_{i-1}}^4}{h_{r_i} + h_{r_{i-1}}}\right) \partial_{rrrr} \phi_{i,j} + \mathcal{O}\left(\frac{h_{r_i}^5 + h_{r_{i-1}}^5}{h_{r_i} + h_{r_{i-1}}}\right), \end{aligned} \tag{4.4}$$

and

$$\begin{aligned} \partial_{rr} \phi_{i,j} = \delta_r^2 \phi_{i,j} - \frac{1}{3}\left(h_{r_i} - h_{r_{i-1}}\right) \partial_{rrr} \phi_{i,j} - \frac{1}{12}\left(\frac{h_{r_i}^3 + h_{r_{i-1}}^3}{h_{r_i} + h_{r_{i-1}}}\right) \partial_{rrrr} \phi_{i,j} \\ - \frac{1}{60}\left(\frac{h_{r_i}^4 - h_{r_{i-1}}^4}{h_{r_i} + h_{r_{i-1}}}\right) \partial_{rrrrr} \phi_{i,j} + \mathcal{O}\left(\frac{h_{r_i}^5 + h_{r_{i-1}}^5}{h_{r_i} + h_{r_{i-1}}}\right). \end{aligned} \tag{4.5}$$

4.2.1 Second-order accurate scheme

Straightforward extension of the formulation discussed in section 2.2 yields the second-order accurate approximation of second-order derivative as

$$\begin{aligned}\partial_{rr}\phi_{i,j} =& 2\left(\frac{(h_{r_i}^2 - h_{r_i}h_{r_{i-1}} + h_{r_{i-1}}^2)}{h_{r_i}^2 + h_{r_{i-1}}^2}(2\delta_r^2\phi_{i,j} - \delta_r\phi_{r_{i,j}})\right.\\ &\left.-\frac{h_{r_i} - h_{r_{i-1}}}{h_{r_i}^2 + h_{r_{i-1}}^2}(\delta_r\phi_{i,j} - \phi_{r_{i,j}})\right) + \mathcal{O}\left((h_{r_i} - h_{r_{i-1}})^2\right),\end{aligned} \tag{4.6}$$

and

$$\begin{aligned}\partial_{\theta\theta}\phi_{i,j} =& 2\left(\frac{(h_{\theta_j}^2 - h_{\theta_j}h_{\theta_{j-1}} + h_{\theta_{j-1}}^2)}{h_{\theta_j}^2 + h_{\theta_{j-1}}^2}(2\delta_\theta^2\phi_{i,j} - \delta_\theta\phi_{\theta_{i,j}})\right.\\ &\left.-\frac{h_{\theta_j} - h_{\theta_{j-1}}}{h_{\theta_j}^2 + h_{\theta_{j-1}}^2}(\delta_\theta\phi_{i,j} - \phi_{\theta_{i,j}})\right) + \mathcal{O}\left((h_{\theta_j} - h_{\theta_{j-1}})^2\right).\end{aligned} \tag{4.7}$$

Once these approximations are achieved, they are used in the CDE (4.1) to obtain its semidiscrete form around the node (i, j) as,

$$a\left.\frac{\partial\phi}{\partial t}\right|_{i,j} + [\mathscr{C}\phi]_{i,j} = f_{i,j}. \tag{4.8}$$

The operator $\mathscr{C}$ is defined as

$$\begin{aligned}[\mathscr{C}\phi]_{i,j} =& -\left(2C_1\delta_r^2 + \frac{2C_2}{r_i^2}\delta_\theta^2 + \frac{C_3}{h_{r_{i-1}}}\delta_r + \frac{C_4}{r_i^2 h_{\theta_{j-1}}}\delta_\theta\right)\phi_{i,j}\\ &+\left(C_1\delta_r + \frac{C_3}{h_{r_{i-1}}} + \mathscr{c}_1\right)\phi_{r_{i,j}} + \left(\frac{C_2}{r_i^2}\delta_\theta + \frac{C_4}{r_i^2 h_{\theta_{j-1}}} + \mathscr{c}_2\right)\phi_{\theta_{i,j}}\end{aligned} \tag{4.9}$$

which is accompanied by the coefficients

$$C_1 = \frac{2(1-\alpha_r+\alpha_r^2)}{(1+\alpha_r^2)}, \quad C_2 = \frac{2(1-\alpha_\theta+\alpha_\theta^2)}{(1+\alpha_\theta^2)}, \quad C_3 = \frac{2(1-\alpha_r)}{(1+\alpha_r^2)}, \quad C_4 = \frac{2(1-\alpha_\theta)}{(1+\alpha_\theta^2)}.$$

In the coefficients C_1, C_2, C_3 and C_4 the terms α_r and α_θ are used to replace the arrays α_{r_i}, $i \in \{1, 2, 3, \ldots, n_r - 2\}$ and α_{θ_j}, $j \in \{1, 2, 3, \ldots, n_\theta - 2\}$ respectively, which are characterized as follows,

$$\begin{aligned}\alpha_{r_i} &= h_{r_{i+1}}/h_{r_i}, \quad i \in \{1, 2, 3, \ldots, n_r - 2\},\\ \alpha_{\theta_j} &= h_{\theta_{j+1}}/h_{\theta_j}, \quad j \in \{1, 2, 3, \ldots, n_\theta - 2\}.\end{aligned}$$

It is fairly evident that the values of α_r and α_θ varies with the change in the values of grid spacing and so are the values of C_i's, $i \in \{1, 2, 3, 4\}$. Since we seek to time march from nth to $(n+1)$th level, we further carry out the temporal discretization of

the unsteady term in equation (4.8). With the aid of Crank-Nicolson approximation, the fully discretized form of CDE (4.1) can be expressed as

$$\left(\frac{2a}{\delta t}+\mathscr{C}\right)\phi_{i,j}^{n+1}=\left(\frac{2a}{\delta t}-\mathscr{C}\right)\phi_{i,j}^{n}+\left(f_{i,j}^{n+1}+f_{i,j}^{n}\right). \tag{4.10}$$

Finally, making use of the operators δ_r, δ_θ, δ_r^2 and δ_θ^2 in $\mathscr{C}$, the algebraic system associated with equation (4.10) can be derived as

$$\begin{aligned}
&\left(\frac{2a}{\delta t}+\widehat{C}_1\right)\phi_{i,j}^{n+1}-\widehat{C}_2\phi_{i+1,j}^{n+1}-\widehat{C}_3\phi_{i-1,j}^{n+1}-\widehat{C}_4\phi_{i,j+1}^{n+1}-\widehat{C}_5\phi_{i,j-1}^{n+1}\\
=&\left(\frac{2a}{\delta t}-\widehat{C}_1\right)\phi_{i,j}^{n}+\widehat{C}_2\phi_{i+1,j}^{n}+\widehat{C}_3\phi_{i-1,j}^{n}+\widehat{C}_4\phi_{i,j+1}^{n}+\widehat{C}_5\phi_{i,j-1}^{n}\\
&-\widehat{C}_6\left(\phi_{r_{i+1,j}}^{n+1}-\phi_{r_{i-1,j}}^{n+1}\right)-\left(\widehat{C}_7+\mathscr{c}_1\right)\phi_{r_{i,j}}^{n+1}\\
&-\widehat{C}_8\left(\phi_{\theta_{i,j+1}}^{n+1}-\phi_{\theta_{i,j-1}}^{n+1}\right)-\left(\widehat{C}_9+\mathscr{c}_2\right)\phi_{\theta_{i,j}}^{n+1}\\
&-\widehat{C}_6\left(\phi_{r_{i+1,j}}^{n}-\phi_{r_{i-1,j}}^{n}\right)-\left(\widehat{C}_7+\mathscr{c}_1\right)\phi_{r_{i,j}}^{n}\\
&-\widehat{C}_8\left(\phi_{\theta_{i,j+1}}^{n}-\phi_{\theta_{i,j-1}}^{n}\right)-\left(\widehat{C}_9+\mathscr{c}_2\right)\phi_{\theta_{i,j}}^{n}\\
&+\left(f_{i,j}^{n+1}+f_{i,j}^{n}\right)
\end{aligned} \tag{4.11}$$

where,

$$\begin{aligned}
\widehat{C}_1=&4\left(\frac{C_1}{\alpha_r h_{r_{i-1}}^2}+\frac{C_2}{\alpha_\theta h_{\theta_{j-1}}^2 r_i^2}\right),\\
\widehat{C}_2=&\frac{1}{(1+\alpha_r)h_{r_{i-1}}^2}\left(\frac{4C_1}{\alpha_r}+C_3\right), &\widehat{C}_3=&\frac{1}{(1+\alpha_r)h_{r_{i-1}}^2}\left(4C_1-C_3\right),\\
\widehat{C}_4=&\frac{1}{(1+\alpha_\theta)h_{\theta_{j-1}}^2 r_i^2}\left(\frac{4C_2}{\alpha_\theta}+C_4\right), &\widehat{C}_5=&\frac{1}{(1+\alpha_\theta)h_{\theta_{j-1}}^2 r_i^2}\left(4C_2-C_4\right),\\
\widehat{C}_6=&\frac{C_1}{(1+\alpha_r)h_{r_{i-1}}}, &\widehat{C}_7=&\frac{C_3}{h_{r_{i-1}}},\\
\widehat{C}_8=&\frac{C_2}{(1+\alpha_\theta)h_{\theta_{j-1}}r_i^2}, &\widehat{C}_9=&\frac{C_4}{h_{\theta_{j-1}}r_i^2}.
\end{aligned}$$

4.2.2 Third-order accurate scheme

In this section, we intend to derive a third-order accurate Padé based compact approximation of the second-order derivative. As established in Chapter 2, the

equation (4.6) with its second-order truncation term can be written as

$$\begin{aligned}\partial_{rr}\phi_{i,j} =& 2\left(\frac{(h_{r_i}^2 - h_{r_i}h_{r_{i-1}} + h_{r_{i-1}}^2)}{h_{r_i}^2 + h_{r_{i-1}}^2}(2\delta_r^2\phi_{i,j} - \delta_r\phi_{r_{i,j}})\right.\\ &\left.-\frac{h_{r_i} - h_{r_{i-1}}}{h_{r_i}^2 + h_{r_{i-1}}^2}(\delta_r\phi_{i,j} - \phi_{r_{i,j}})\right) + \frac{1}{12}(h_{r_i} - h_{r_{i-1}})^2\partial_{rrrr}\phi_{i,j}\\ &+ \mathcal{O}\left(\frac{(h_{r_i} - h_{r_{i-1}})(2h_{r_i}^4 - 2h_{r_i}^3h_{r_{i-1}} + 3h_{r_i}^2h_{r_{i-1}}^2 - 2h_{r_i}h_{r_{i-1}}^3 + 2h_{r_{i-1}}^4)}{(h_{r_i}^2 + h_{r_{i-1}}^2)}\right).\end{aligned} \tag{4.12}$$

Here, we note that the above second-order discretization not only attains optimal fourth-order convergence on uniform grid but also its leading truncation error term $\frac{1}{12}(h_{r_i} - h_{r_{i-1}})^2\partial_{rrrr}\phi_{i,j}$, as seen in equation (4.12), converges to zero quadratically as we move from nonuniform to uniform grid. Again, substituting $\partial_{rrr}\phi_{i,j}$ from equation (4.4) in equation (4.5), the following second order approximation for the second-order derivative can be obtained

$$\begin{aligned}\partial_{rr}\phi_{i,j} =& \frac{h_{r_i}^2 - h_{r_i}h_{r_{i-1}} + h_{r_{i-1}}^2}{h_{r_i}h_{r_{i-1}}}\delta_r^2\phi_{i,j} - \frac{2(h_{r_i} - h_{r_{i-1}})}{h_{r_i}h_{r_{i-1}}}(\delta_r\phi_{i,j} - \phi_{r_{i,j}})\\ &- \frac{1}{12}h_{r_i}h_{r_{i-1}}\partial_{rrrr}\phi_{i,j} + \mathcal{O}\left((h_{r_{i-1}} - h_{r_i})h_{r_i}h_{r_{i-1}}\right).\end{aligned} \tag{4.13}$$

It is easy to see that equation (4.13) reverts back to standard central approximation of order two on uniform grid. Next, eliminating the fourth-order derivative from equations (4.12) and (4.13), we arrive at the following discretization of the second-order derivative with third-order truncation term on nonuniform grid as

$$\begin{aligned}\partial_{rr}\phi_{i,j} =& 2\left\{\left(\frac{2h_{r_i}h_{r_{i-1}}}{h_{r_i}^2 + h_{r_{i-1}}^2} + \frac{(h_{r_i} - h_{r_{i-1}})^2}{2h_{r_i}h_{r_{i-1}}}\right)\delta_r^2\phi_{i,j} - \frac{h_{r_i}h_{r_{i-1}}}{h_{r_i}^2 + h_{r_{i-1}}^2}\delta_r\phi_{r_{i,j}}\right.\\ &\left.-\frac{(h_{r_i} - h_{r_{i-1}})}{h_{r_i}^2 - h_{r_i}h_{r_{i-1}} + h_{r_{i-1}}^2}\left(\frac{h_{r_i}h_{r_{i-1}}}{h_{r_i}^2 + h_{r_{i-1}}^2} + \frac{(h_{r_i} - h_{r_{i-1}})^2}{h_{r_i}h_{r_{i-1}}}\right)(\delta_r\phi_{i,j} - \phi_{r_{i,j}})\right\}\\ &+ \mathcal{O}\left(\frac{(h_{r-i} - h_{r_i})h_{r_i}h_{r_{i-1}}(h_{r_i}^2 + h_{r_i}h_{r_{i-1}} + h_{r_{i-1}}^2)}{(h_{r_i}^2 + h_{r_{i-1}}^2)}\right).\end{aligned} \tag{4.14}$$

It is quite evident that on uniform grid the above approximation shall revert back to compact fourth-order approximation presented in [130]. Compared to discretization in equation (4.12), approximation in equation (4.14) possesses a higher-order truncation term and the order of approximation is optimal on nonuniform compact

stencil. We shall explore relative convergence characteristics of the schemes from equations (4.12) and (4.14) in subsequent sections in the context of CDE and N-S equations. Necessary Padé type third-order approximation on nonuniform grids shall be discussed in the later part of this section and shall be identically employed for both equations (4.12) and (4.14).

Again, following a similar course of action in the θ-direction, we get

$$\begin{aligned}\partial_{\theta\theta}\phi_{i,j} =& 2\left\{\left(\frac{2h_{\theta_j}h_{\theta_{j-1}}}{h_{\theta_j}^2+h_{\theta_{j-1}}^2}+\frac{(h_{\theta_j}-h_{\theta_{j-1}})^2}{2h_{\theta_j}h_{\theta_{j-1}}}\right)\delta_\theta^2\phi_{i,j}-\frac{h_{\theta_j}h_{\theta_{j-1}}}{h_{\theta_j}^2+h_{\theta_{j-1}}^2}\delta_\theta\phi_{\theta_{i,j}}\right.\\ &\left.-\frac{(h_{\theta_j}-h_{\theta_{j-1}})}{h_{\theta_j}^2-h_{\theta_j}h_{\theta_{j-1}}+h_{\theta_{j-1}}^2}\left(\frac{h_{\theta_j}h_{\theta_{j-1}}}{h_{\theta_j}^2+h_{\theta_{j-1}}^2}+\frac{(h_{\theta_j}-h_{\theta_{j-1}})^2}{h_{\theta_j}h_{\theta_{j-1}}}\right)(\delta_\theta\phi_{i,j}-\phi_{\theta_{i,j}})\right\}\\ &+\mathcal{O}\left(\frac{h_{\theta_j}h_{\theta_{j-1}}(h_{\theta_j}^3-h_{\theta_{j-1}}^3)}{(h_{\theta_j}^2+h_{\theta_{j-1}}^2)}\right).\end{aligned} \tag{4.15}$$

Making use of these spatial approximations, the CDE (4.1) around the node (i,j) can be expressed in the following semidiscrete form,

$$a\left.\frac{\partial\phi}{\partial t}\right|_{i,j}+[\mathscr{D}\phi]_{i,j}=f_{i,j}. \tag{4.16}$$

The operator $\mathscr{D}$ is defined as

$$\begin{aligned}[\mathscr{D}\phi]_{i,j} =& -\left(2D_1\delta_r^2+\frac{2D_2}{r_i^2}\delta_\theta^2+\frac{D_3}{h_{r_{i-1}}}\delta_r+\frac{D_4}{r_i^2h_{\theta_{j-1}}}\delta_\theta\right)\phi_{i,j}\\ &+\left(\frac{D_3}{h_{r_{i-1}}}+D_5\delta_r+\mathscr{c}_1\right)\phi_{r_{i,j}}+\left(\frac{D_4}{r_i^2h_{\theta_{j-1}}}+\frac{D_6}{r_i^2}\delta_\theta+\mathscr{c}_2\right)\phi_{\theta_{i,j}}\end{aligned} \tag{4.17}$$

where the coefficients are given as

$$\begin{aligned}D_1 &= \frac{2\alpha_r}{1+\alpha_r^2}+\frac{(1-\alpha_r)^2}{2\alpha_r},\\ D_2 &= \frac{2\alpha_\theta}{1+\alpha_\theta^2}+\frac{(1-\alpha_\theta)^2}{2\alpha_\theta},\\ D_3 &= \frac{2(1-\alpha_r)}{(1-\alpha_r+\alpha_r^2)}\left\{\frac{\alpha_r}{(1+\alpha_r^2)}+\frac{(1-\alpha_r)^2}{\alpha_r}\right\},\\ D_4 &= \frac{2(1-\alpha_\theta)}{(1-\alpha_\theta+\alpha_\theta^2)}\left\{\frac{\alpha_\theta}{(1+\alpha_\theta^2)}+\frac{(1-\alpha_\theta)^2}{\alpha_\theta}\right\},\\ D_5 &= \frac{2}{1+\alpha_r^2}\\ D_6 &= \frac{2}{1+\alpha_\theta^2}.\end{aligned}$$

The operators δ_r, δ_θ, δ_r^2 and δ_θ^2 along with Crank-Nicolson approximation yields

the fully discretized form of equation (4.1) as

$$
\begin{aligned}
&\left(\frac{2a}{\delta t}+\widehat{D}_1\right)\phi_{i,j}^{n+1}-\widehat{D}_2\phi_{i+1,j}^{n+1}-\widehat{D}_3\phi_{i-1,j}^{n+1}-\widehat{D}_4\phi_{i,j+1}^{n+1}-\widehat{D}_5\phi_{i,j-1}^{n+1}\\
&=\left(\frac{2a}{\delta t}-\widehat{D}_1\right)\phi_{i,j}^{n}+\widehat{D}_2\phi_{i+1,j}^{n}+\widehat{D}_3\phi_{i-1,j}^{n}+\widehat{D}_4\phi_{i,j+1}^{n}+\widehat{D}_5\phi_{i,j-1}^{n}\\
&\quad-\widehat{D}_6\left(\phi_{r_{i+1,j}}^{n+1}-\phi_{r_{i-1,j}}^{n+1}\right)-\left(\widehat{D}_7+\mathscr{c}_1\right)\phi_{r_{i,j}}^{n+1}\\
&\quad-\widehat{D}_8\left(\phi_{\theta_{i,j+1}}^{n+1}-\phi_{\theta_{i,j-1}}^{n+1}\right)-\left(\widehat{D}_9+\mathscr{c}_2\right)\phi_{\theta_{i,j}}^{n+1}\\
&\quad-\widehat{D}_6\left(\phi_{r_{i+1,j}}^{n}-\phi_{r_{i-1,j}}^{n}\right)-\left(\widehat{D}_7+\mathscr{c}_1\right)\phi_{r_{i,j}}^{n}\\
&\quad-\widehat{D}_8\left(\phi_{\theta_{i,j+1}}^{n}-\phi_{\theta_{i,j-1}}^{n}\right)-\left(\widehat{D}_9+\mathscr{c}_2\right)\phi_{\theta_{i,j}}^{n}\\
&\quad+\left(f_{i,j}^{n+1}+f_{i,j}^{n}\right)
\end{aligned}
\tag{4.18}
$$

where,

$$
\begin{aligned}
\widehat{D}_1 &= 4\left(\frac{D_1}{\alpha_r h_{r_{i-1}}^2}+\frac{D_2}{\alpha_\theta h_{\theta_{j-1}}^2 r_i^2}\right),\\
\widehat{D}_2 &= \frac{1}{(1+\alpha_r)h_{r_{i-1}}^2}\left(\frac{4D_1}{\alpha_r}+D_3\right), & \widehat{D}_3 &= \frac{1}{(1+\alpha_r)h_{r_{i-1}}^2}\left(4D_1-D_3\right),\\
\widehat{D}_4 &= \frac{1}{(1+\alpha_\theta)h_{\theta_{j-1}}^2 r_i^2}\left(\frac{4D_2}{\alpha_\theta}+D_4\right), & \widehat{D}_5 &= \frac{1}{(1+\alpha_\theta)h_{\theta_{j-1}}^2 r_i^2}\left(4D_2-D_4\right),\\
\widehat{D}_6 &= \frac{D_5}{(1+\alpha_r)h_{r_{i-1}}}, & \widehat{D}_7 &= \frac{D_3}{h_{r_{i-1}}},\\
\widehat{D}_8 &= \frac{D_6}{(1+\alpha_\theta)h_{\theta_{j-1}}r_i^2}, & \widehat{D}_9 &= \frac{D_4}{h_{\theta_{j-1}}r_i^2}.
\end{aligned}
$$

The coefficients $\widehat{C}_i$'s and $\widehat{D}_i$'s, $i \in \{1,2,3,\ldots,9\}$, of the algebraic equations (4.11) and (4.18) depend entirely on the values of grid spacings and they remain unchanged throughout the computation once the grid is set up. Therefore, similar to the previous approach, for situations with constant convection and diffusion coefficients the current scheme also offers the inherent benefit of dealing with resulting system of equations containing constant coefficients only. Further, one can easily notice that the discrete operator $\mathscr{C}$ and $\mathscr{D}$ also contain the radial and tangential derivatives of the flow variables, which need to be approximated up to the appropriate order of accuracy. In this aspect, we generalize the Padé scheme [95] to obtain the following

approximations of the spatial derivatives on nonuniform polar grids.

$$\left(1+\frac{h_{r_i}h_{r_{i-1}}}{6}\delta_r^2\right)\phi_{r_{i,j}} = \left(\delta_r - \frac{h_{r_i}-h_{r_{i-1}}}{2}\delta_r^2\right)\phi_{i,j} + \mathcal{O}\left((h_{r_i}-h_{r_{i-1}})(3h_{r_i}^2+h_{r_i}h_{r_{i-1}}+3h_{r_{i-1}}^2)\right), \tag{4.19}$$

and

$$\left(1+\frac{h_{\theta_j}h_{\theta_{j-1}}}{6}\delta_\theta^2\right)\phi_{\theta_{i,j}} = \left(\delta_\theta - \frac{h_{\theta_j}-h_{\theta_{j-1}}}{2}\delta_\theta^2\right)\phi_{i,j} + \mathcal{O}\left((h_{\theta_j}-h_{\theta_{j-1}})(3h_{\theta_j}^2+h_{\theta_j}h_{\theta_{j-1}}+3h_{\theta_{j-1}}^2)\right). \tag{4.20}$$

Subsequently, we obtain the corresponding algebraic system for equations (4.19) and (4.20) as

$$\phi_{r_{i+1,j}}^{n+1} + 2\left(1+\alpha_r\right)\phi_{r_{i,j}}^{n+1} + \alpha_r\phi_{r_{i-1,j}}^{n+1} = \frac{3}{\alpha_r h_{r_{i-1}}}\left(\phi_{i+1,j}^{n+1} - (1-\alpha_r^2)\phi_{i,j}^{n+1} - \alpha_r^2\phi_{i-1,j}^{n+1}\right), \tag{4.21}$$

and

$$\phi_{\theta_{i,j+1}}^{n+1} + 2\left(1+\alpha_\theta\right)\phi_{\theta_{i,j}}^{n+1} + \alpha_\theta\phi_{\theta_{i,j-1}}^{n+1} = \frac{3}{\alpha_\theta h_{\theta_{j-1}}}\left(\phi_{i,j+1}^{n+1} - (1-\alpha_\theta^2)\phi_{i,j}^{n+1} - \alpha_\theta^2\phi_{i,j-1}^{n+1}\right) \tag{4.22}$$

respectively.

As the present scheme carries the flow gradients as variables, it is vital to approximate them at the boundary points. Moreover, in many situations, due to the lack of exact values of the flow variables at the boundary, we must resort to the one-sided approximations of the first-order derivatives. This is done by introducing the following discretizations:

Along the tangential direction, $\forall 1 \leq j \leq n_\theta$

$$\phi_{r_{1,j}} = -\frac{h_{r_1}}{h_{r_2}(h_{r_1}+h_{r_2})}\phi_{3,j} + \frac{h_{r_1}+h_{r_2}}{h_{r_1}h_{r_2}}\phi_{2,j} - \frac{2h_{r_1}+h_{r_2}}{h_{r_1}(h_{r_1}+h_{r_2})}\phi_{1,j} + \mathcal{O}\left(h_{r_2}(h_{r_1}+h_{r_2})\right), \tag{4.23a}$$

$$\phi_{r_{n_r,j}} = \frac{h_{r_{n_r-1}}}{h_{r_{n_r-2}}(h_{r_{n_r-1}}+h_{r_{n_r-2}})}\phi_{n_r-2,j} - \frac{h_{r_{n_r-1}}+h_{r_{n_r-2}}}{h_{r_{n_r-1}}h_{r_{n_r-2}}}\phi_{n_r-1,j} + \frac{2h_{r_{n_r-1}}+h_{r_{n_r-2}}}{h_{r_{n_r-1}}(h_{r_{n_r-1}}+h_{r_{n_r-2}})}\phi_{n_r,j} + \mathcal{O}\left(h_{r_{n_r-1}}(h_{r_{n_r-1}}+h_{r_{n_r-2}})\right), \tag{4.23b}$$

Along the radial direction, $\forall 1 \leq i \leq n_r$

$$\begin{aligned}\phi_{\theta_{i,1}} =& -\frac{h_{\theta_1}}{h_{\theta_2}(h_{\theta_1}+h_{\theta_2})}\phi_{i,3} + \frac{h_{\theta_1}+h_{\theta_2}}{h_{\theta_1}h_{\theta_2}}\phi_{i,2} - \frac{2h_{\theta_1}+h_{\theta_2}}{h_{\theta_1}(h_{\theta_1}+h_{\theta_2})}\phi_{i,1} \\ &+ \mathcal{O}\left(h_{\theta_2}(h_{\theta_1}+h_{\theta_2})\right), \end{aligned} \tag{4.24a}$$

$$\begin{aligned}\phi_{\theta_{i,n_\theta}} =& \frac{h_{\theta_{n_\theta-1}}}{h_{\theta_{n_\theta-2}}(h_{\theta_{n_\theta-1}}+h_{\theta_{n_\theta-2}})}\phi_{i,n_\theta-2} - \frac{h_{\theta_{n_\theta-1}}+h_{\theta_{n_\theta-2}}}{h_{\theta_{n_\theta-1}}h_{\theta_{n_\theta-2}}}\phi_{i,n_\theta-1} \\ &+ \frac{2h_{\theta_{n_\theta-1}}+h_{\theta_{n_\theta-2}}}{h_{\theta_{n_\theta-1}}(h_{\theta_{n_\theta-1}}+h_{\theta_{n_\theta-2}})}\phi_{i,n_\theta} + \mathcal{O}\left(h_{\theta_{n_\theta-1}}(h_{\theta_{n_\theta-1}}+h_{\theta_{n_\theta-2}})\right). \end{aligned} \tag{4.24b}$$

4.3 Solution of algebraic system

The developed FD approximations (4.11) and (4.18) yields a system of equations, which in matrix form can be written as

$$M_1\Phi^{(n+1)} = F_1\left(\Phi^{(n)}, \Phi_r^{(n)}, \Phi_\theta^{(n)}, \Phi_r^{(n+1)}, \Phi_\theta^{(n+1)}\right), \tag{4.25}$$

with

$$\begin{aligned} \Phi &= (\phi_{1,1}, \phi_{1,2}, \ldots, \phi_{1,n_\theta}, \phi_{2,1}, \phi_{2,2}, \ldots, \phi_{2,n_\theta}, \ldots, \phi_{n_r,n_\theta})^T, \\ \Phi_r &= \left(\phi_{r_{1,1}}, \phi_{r_{1,2}}, \ldots, \phi_{r_{1,n_\theta}}, \phi_{r_{2,1}}, \phi_{r_{2,2}}, \ldots, \phi_{r_{2,n_\theta}}, \ldots, \phi_{r_{n_r,n_\theta}}\right)^T \\ \text{and} \quad \Phi_\theta &= \left(\phi_{\theta_{1,1}}, \phi_{\theta_{1,2}}, \ldots, \phi_{\theta_{1,n_\theta}}, \phi_{\theta_{2,1}}, \phi_{\theta_{2,2}}, \ldots, \phi_{\theta_{2,n_\theta}}, \ldots, \phi_{\theta_{n_r,n_\theta}}\right)^T. \end{aligned}$$

Here, the matrix M_1 is a sparse nonsymmetric matrix with five nonzero diagonals. As stated in section 4.2, algebraic system of equations involves only constant coefficients once the grid is laid out. Thus on a grid of size $n_r \times n_\theta$, the coefficient matrix M_1 only deals with constant entries. Although the system appears to have a large dimension $3n_rn_\theta \times 3n_rn_\theta$, one only needs to handle a system of size $n_r \times n_\theta$ while employing a predictor-corrector method [130, 134].

Similarly, matrix representation of equation (4.21) and equation (4.22) are

$$M_2\Phi_r^{(n)} = F_2\left(\Phi^{(n)}\right) \tag{4.26}$$

and

$$M_3\Phi_\theta^{(n)} = F_3\left(\Phi^{(n)}\right) \tag{4.27}$$

respectively. M_2 and M_3 are tri-diagonal matrices and hence systems (4.26) and

(4.27) are very amenable to efficient computation. The algorithmic procedure adopted at this stage is same as delineated in [130, 134].

4.4 Numerical examples

To examine the accuracy and effectiveness of the present scheme on nonuniform polar grids, it has been employed to five diverse problems of varying complexities. Verification study is carried out using two problems *viz.* Navier-Stokes equations with an analytical solution and convection-diffusion of Gaussian pulse. We study the efficiency of the scheme in handling complex flow patterns by solving the driven polar cavity problem. Subsequently, we enter the field of heat transfer by tackling the problem of heat convection in an annulus. Finally, we carry out a comprehensive simulation of fluid flow and heat transfer around a circular cylinder. The intention behind selecting these problems is to highlight the inherent flexibility of nonuniform grids whereby certain portions of the solution domain can be better resolved with grid clustering. Furthermore, the overwhelming number of numerical solutions present in the literature gives us the leverage to compare the numerical solutions of the present scheme with the existing ones. All the computations are executed on an Intel i7-based PC with 3.40 GHz CPU and 32 GB RAM. The tolerance for inner and outer iterations is set to be $1.0e-10$.

4.4.1 Problem 1: Navier-Stokes equations with analytical solution

We first apply the second-order accurate formulation given in equation (4.11) and third-order accurate scheme given in equation (4.18) on 2D steady incompressible viscous fluid flow in the unit circular domain $(0,1)\times[0,2\pi]$. The flow is governed by the steady-state N-S equations in the polar coordinate system given as,

$$\begin{cases} \omega_{rr}+\dfrac{1}{r}\omega_r+\dfrac{1}{r^2}\omega_{\theta\theta}=Re\left(u\omega_r+\dfrac{v}{r}\omega_\theta\right), & \text{(4.28a)}\\ \psi_{rr}+\dfrac{1}{r}\psi_r+\dfrac{1}{r^2}\psi_{\theta\theta}=-\omega, & \text{(4.28b)} \end{cases}$$

where $u(r,\theta) = \frac{1}{r}\psi_\theta$ is the radial velocity component and $v(r,\theta) = -\psi_r$ is the tangential velocity component. For $Re = 0$, the exact solution of the equation (4.28) is obtained to be

$$\psi(r,\theta) = \left(2r^2 - r^4\right)\cos 2\theta, \tag{4.29a}$$

$$\omega(r,\theta) = 12r^2\cos 2\theta. \tag{4.29b}$$

The Dirichlet boundary conditions are derived from the exact solution given in equation (4.29) and are used along all boundaries.

We solve the problem directly on polar grids of three different sizes 21×21, 41×41 and 81×81 generated by $x = r\cos\theta$ and $y = r\sin\theta$. The grid spacing in the tangential direction has been kept uniform while in the radial direction nonuniform grids are generated using a trigonometric function analogous to equation (2.28) given by

$$r_i = L_r\left\{\frac{i}{n_r} + \frac{\lambda_r}{\Theta_r}\sin\left(\frac{\Theta_r i}{n_r}\right)\right\}. \tag{4.30}$$

Here, $L_r = 1.0$. The grids are clustered near the centre and boundary of the domain by using $\Theta_r = \pi$ while the clustering parameter λ_r is set to be 0.6.

To establish the efficiency of the methods further, quantitative analysis has been carried out in Tables 4.1 and 4.2. The tables contain L_1, L_2 and L_∞-norm errors for ψ and ω. In these tables we have also assessed the spatial order of convergence of the newly developed scheme. To our delight, the present methods carry nearly fourth-order of convergence in all the three norms. Additionally, to provide a sense of increase in computational cost with increase in grid size the relative CPU time is also been presented in Tables 4.1 and 4.2. It is seen that with grid points increasing by a factor of four from 21×21 to 41×41 the computational time increases twenty fold for both second and third order schemes. With subsequent refinement of mesh from 41×41 to 81×81, we notice approximately 6 fold and 11 fold increase in relative computational time for second and third order schemes respectively. This increase might be slower convergence of the associated system of algebraic equations. This in turn could relate to increased clustering of the grid at specific regions.

Fig. 4.2a and 4.2b depict the contours of exact solution and numerical solu-

Table 4.1: Problem 1: L_1, L_2 and L_∞-norm errors of ψ and ω at different grids and spatial rate of convergence computed using the second-order accurate scheme.

		21×21	order	41×41	order	81×81
ψ	L_1	5.288883e-5	3.95	3.425683e-6	3.98	2.170506e-7
	L_2	7.294481e-5	3.96	4.672874e-6	3.99	2.942073e-7
	L_∞	1.838957e-4	3.96	1.178966e-5	3.99	7.412592e-7
ω	L_1	3.048381e-4	3.95	1.972423e-5	3.98	1.252045e-6
	L_2	4.125221e-4	3.96	2.645734e-5	3.99	1.666696e-6
	L_∞	1.008048e-3	3.97	6.436643e-5	3.99	4.045326e-6
CPU time		1.0		19.98		128.58

Table 4.2: Problem 1: L_1, L_2 and L_∞-norm errors of ψ and ω at different grids and spatial rate of convergence computed using the third-order accurate scheme.

		21×21	order	41×41	order	81×81
ψ	L_1	5.336185e-5	3.95	3.455915e-6	3.98	2.189649e-7
	L_2	7.359994e-5	3.96	4.714214e-6	3.99	2.968013e-7
	L_∞	1.855857e-4	3.96	1.189500e-5	3.99	7.478539e-7
ω	L_1	3.048408e-4	3.95	1.972424e-5	3.98	1.252045e-6
	L_2	4.125248e-4	3.96	2.645734e-5	3.99	1.666696e-6
	L_∞	1.008052e-3	3.97	6.436644e-5	3.99	4.045326e-6
CPU time		1.07		21.47		238.26

tions for ψ and ω respectively. For both the flow variables, the exact and numerically approximated contours are seen to be indistinguishable from each other, which demonstrates the accuracy of the schemes.

4.4.2 Problem 2: Convection and diffusion of Gaussian pulse

This validation study is intended to capture the unsteady convection and diffusion of a Gaussian pulse in the domain $[0, 2] \times [0, \frac{\pi}{2}]$. This flow situation is governed by equation (4.1) and is equipped with the analytical solution

$$\phi(r, \theta, t) = -\frac{1}{4t+1} \exp\left[\frac{(ar\cos\theta - c_1 t - 0.1a)^2}{a(4t+1)} + \frac{(ar\sin\theta - c_2 t - 0.1a)^2}{a(4t+1)}\right].$$

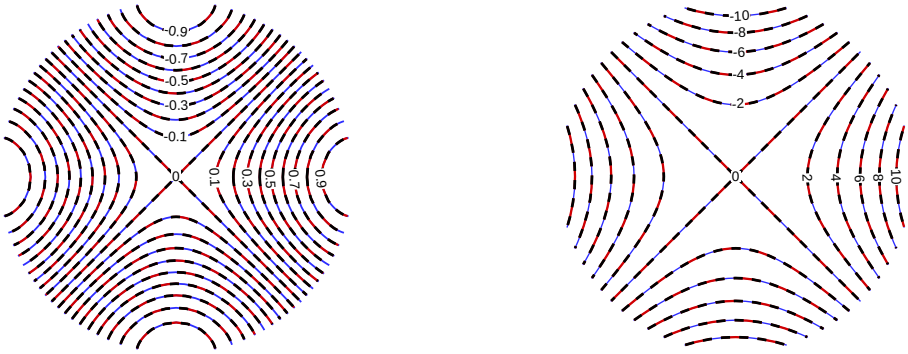

(a) (b)

Fig. 4.2: Problem 1: Exact and numerical contour plots of (a) ψ and (b) ω (black: exact solution; blue: numerical solution obtained using second-order accurate scheme; red: numerical solution obtained using third-order accurate scheme).

(4.31)

Equation (4.31) directly provides the initial condition and Dirichlet boundary conditions. At $t = 0$, equation (4.31) represents a pulse of unit height centred at (0.1,0.1) and as time advances it moves along the line $\theta = \dfrac{\pi}{4}$.

The convection coefficients have been set at values $c_1 = c_2 = 150$ for the current study. Further, a=100 and $\delta t = 2.5e-5$ are kept fixed. A nonuniform grid has been used in the tangential direction that clusters in the vicinity of $\theta = \dfrac{\pi}{4}$ and uniform grid spacing has been maintained along the radial direction. The nonuniform grid is generated using the trigonometric function

$$\theta_j = L_\theta \left\{ \frac{j}{n_\theta} + \frac{\lambda_\theta}{\Theta_\theta} \sin\left(\frac{j\Theta_\theta}{n_\theta} \right) \right\}. \tag{4.32}$$

A typical 33×33 grid so formed has been displayed in Fig. 4.3a. The degree of clustering is decided by the clustering parameter $\lambda_\theta = 0.6$. Values of the other constants have been taken as $L_\theta = \dfrac{\pi}{2}$ and $\Theta_\theta = 2\pi$.

Comparisons between the numerical and exact solutions at two different times $t = 0.25$ and $t = 0.50$ are presented in Fig. 4.3b and 4.3c respectively. The numerical solutions are seen to be almost indistinguishable from the exact solution conforming to the efficiency of the present scheme to capture the moving pulse accurately. L_1, L_2, and L_∞-norm errors at each time step for the entire computation time are

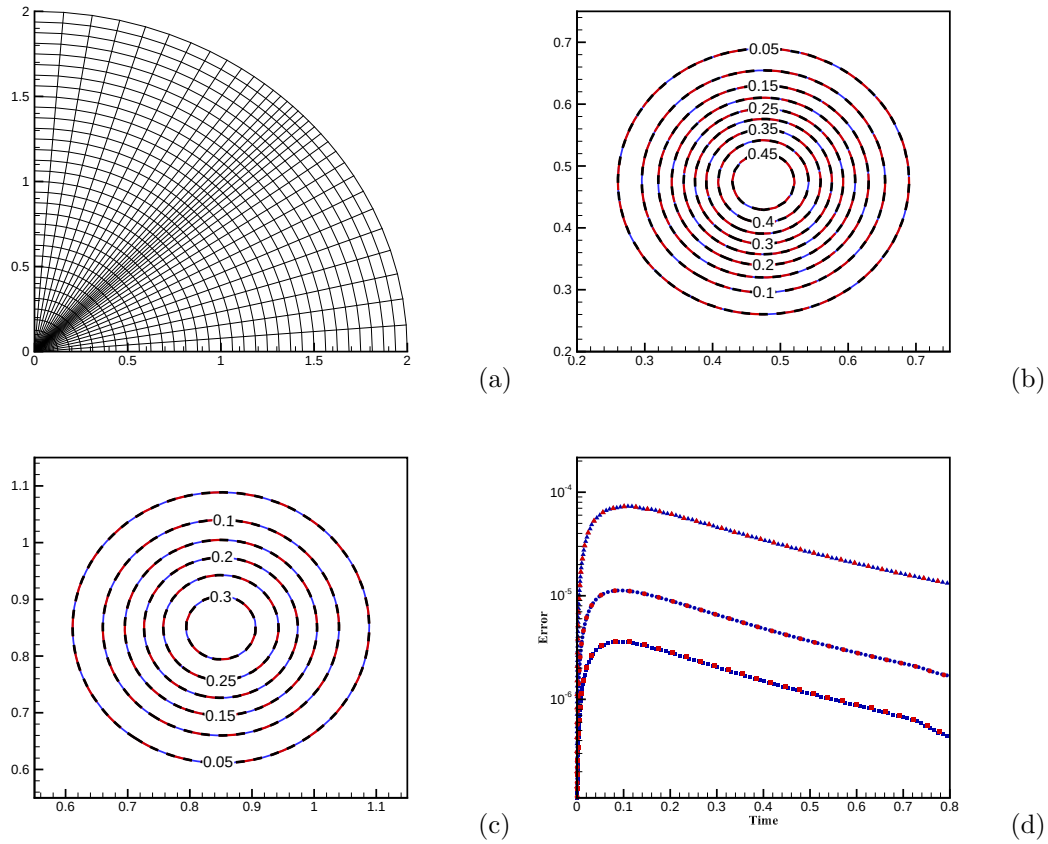

Fig. 4.3: Problem 2: (a) Typical 33×33 grids ; exact and numerical contour plots of the Gaussian pulse at (b) $t = 0.25$, (c) $t = 0.50$; (d) time evolution of L_1 (square), L_2 (circle) and L_∞ (triangle)-norm errors (black: exact solution; blue: numerical solution obtained using second-order accurate scheme; red: numerical solution obtained using third-order accurate scheme).

presented in Fig. 4.3d. The similar temporal decaying nature of all three norm errors justifies the convergence of the present scheme.

A quantitative assessment of the numerical solutions has been carried out in Tables 4.3 to 4.6. In Tables 4.3 and 4.4, we have calculated the spatial order of convergence using second-order accurate scheme and third-order accurate scheme respectively, for the computations done on three grids of different sizes 33×33, 65×65 and 129×129 with $\delta t = 2.5e - 5$. For the temporal rate of convergence computations are carried out with $\delta t = 0.02$, $\delta t = 0.01$ and $\delta t = 0.005$ on a 129×129 grid. The clustering parameter has been kept at $\lambda_\theta = 0.1$ to make spatial error much smaller compared to the temporal error. Computed errors at various times along

Table 4.3: Problem 2: L_1, L_2 and L_∞-norm errors of ϕ at different grids and spatial rate of convergence, computed using second-order accurate scheme.

Time		33×33	order	65×65	order	129×129
0.25	L_1	7.337950e-4	4.20	4.000405e-5	4.02	2.458262e-6
	L_2	2.248532e-3	4.13	1.285689e-4	4.06	7.682233e-6
	L_∞	1.353525e-2	3.92	8.922124e-4	4.07	5.329986e-5
CPU time		1.0		6.76		75.34
0.50	L_1	3.322361e-4	4.16	1.862575e-5	4.00	1.160263e-6
	L_2	1.027532e-3	4.10	6.000015e-5	4.04	3.639986e-6
	L_∞	6.769672e-3	4.02	4.174938e-4	3.98	2.645134e-5
CPU time		2.31		14.81		157.0

Table 4.4: Problem 2: L_1, L_2 and L_∞-norm errors of ϕ at different grids and spatial rate of convergence, computed using third-order accurate scheme.

Time		33×33	order	65×65	order	129×129
0.25	L_1	7.337756e-4	4.20	3.990618e-5	4.06	2.390596e-6
	L_2	2.248623e-3	4.13	1.285848e-4	4.06	7.687400e-6
	L_∞	1.353756e-2	3.92	8.920667e-4	4.07	5.328468e-5
CPU time		6.22		98.01		592.28
0.50	L_1	3.322961e-4	4.16	1.859497e-5	4.04	1.132402e-6
	L_2	1.027676e-3	4.10	6.002334e-5	4.04	3.646823e-6
	L_∞	6.769691e-3	4.02	4.174422e-4	3.98	2.643113e-5
CPU time		15.22		204.50		1225.30

with the temporal accuracy have been presented in Tables 4.5 and 4.6. Both the schemes show near fourth-order convergences in space and a temporal accuracy of order two.

Numerical results presented in Problem 1 and Problem 2 reveal that both theoretically second-order and third-order schemes report optimal fourth-order convergence for the nonuniform grids considered. Indeed, there is little difference between the results churned out by the numerical schemes. In the context of the two problems, one can see comparable behaviour of numerical solutions computed using the sec-

Table 4.5: Problem 2: L_1, L_2 and L_∞-norm errors of ϕ at different values of δt and temporal rate of convergence, computed using second-order accurate scheme.

Time		$\delta t = 0.02$	order	$\delta t = 0.01$	order	$\delta t = 0.005$
0.50	L_1	1.223078e-3	2.02	3.021393e-4	2.00	7.539567e-5
	L_2	4.799785e-3	2.01	1.192406e-3	2.00	2.976308e-4
	L_∞	4.591702e-2	2.07	1.096137e-2	2.03	2.684967e-3
CPU time		1.61		1.11		1.0
0.80	L_1	6.590089e-4	2.10	1.544171e-4	2.03	3.775900e-5
	L_2	3.082619e-3	2.05	7.453994e-4	2.02	1.837000e-4
	L_∞	3.164249e-2	2.06	7.566624e-3	2.03	1.850045e-3
CPU time		3.48		2.37		2.06

Table 4.6: Problem 2: L_1, L_2 and L_∞-norm errors of ϕ at different values of δt and temporal rate of convergence, computed using third-order accurate scheme.

Time		$\delta t = 0.02$	order	$\delta t = 0.01$	order	$\delta t = 0.005$
0.50	L_1	2.098479e-3	2.01	5.204632e-4	2.00	1.299927e-4
	L_2	6.556053e-3	2.01	1.632436e-3	2.00	4.077176e-4
	L_∞	4.591483e-2	2.07	1.096071e-2	2.03	2.684826e-3
CPU time		12.03		10.17		14.61
0.80	L_1	1.202700e-3	2.09	2.823366e-4	2.03	6.907145e-5
	L_2	4.319963e-3	2.05	1.045744e-3	2.02	2.577760e-4
	L_∞	3.164084e-2	2.06	7.566229e-3	2.03	1.849941e-3
CPU time		26.67		22.79		34.23

ond and the third-order accurate schemes. This could be attributed to truncation error terms associated with both the second and third-order schemes as discussed earlier especially for grids where spacing varies gradually. Similar to the steady case discussed in previous problem, here also it is seen that there is six to fifteen fold increase in relative computational time as the number of grid points increase by a factor of four for both the schemes. Further, Tables 4.3 and 4.4 reveal third-order scheme is a bit more computationally expensive and could be attributed to increased computations associated with the determination of the coefficients. In Tables 4.5 and 4.6 it is interesting to note that even with smaller temporal step size both the

schemes report comparable CPU time to simulate up to time 0.8. It is felt that with smaller δt convergence of associated system is faster as smaller δt tends to decrease the condition number of the system. But the same can only be confirmed after a detailed study. Thus, keeping relevant to the previous chapters, we compute the succeeding problems by adopting the second-order accurate scheme only.

4.4.3 Problem 3: Driven polar cavity

Flow inside a polar cavity is also been simulated using the present scheme. This problem is governed by the transient form of N-S equations (4.28) which can be given as

$$\begin{cases} \omega_t = \dfrac{1}{Re}\left(\omega_{rr} + \dfrac{1}{r}\omega_r + \dfrac{1}{r^2}\omega_{\theta\theta}\right) - \left(u\omega_r + \dfrac{v}{r}\omega_\theta\right), & \text{(4.33a)} \\ \omega = -\left(\psi_{rr} + \dfrac{1}{r}\psi_r + \dfrac{1}{r^2}\psi_{\theta\theta}\right). & \text{(4.33b)} \end{cases}$$

This particular problem was first studies experimentally and numerically by Fuchs and Tillmark [45] and it has been considered extensively in various studies ever since to validate numerical schemes, particularly for physical domains with circular arc as boundaries [26, 93, 123, 132, 176].

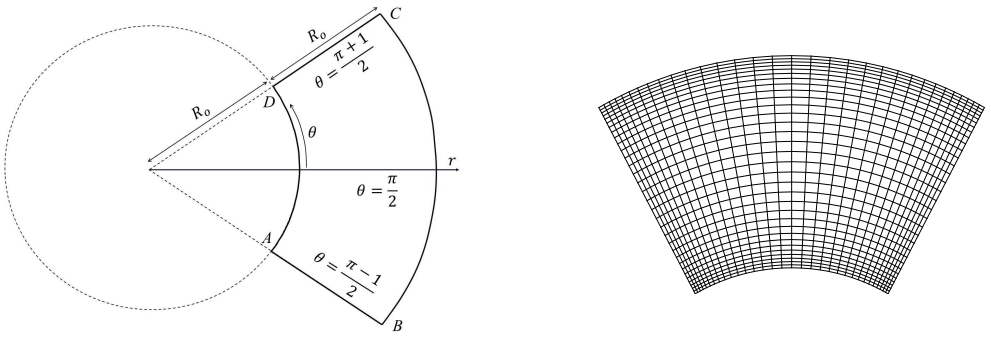

(a) (b)

Fig. 4.4: Problem 3: (a) Schematic diagram and (b) typical 33×33 centrosymmetric polar grid for flow inside a polar cavity.

The problem is described in the annular cavity $[1, 2] \times \left[\dfrac{\pi - 1}{2}, \dfrac{\pi + 1}{2}\right]$. An illustration of the problem is presented in Fig. 4.4a. The domain of driven polar cavity

problem is the region $ABCD$: the length $AB = DC$ is equal to radius $R_0 = 1$ of the inner circle. The circular arc $\widehat{DA}$ rotates uniformly maintaining a unit velocity in the clockwise direction. This rotation drives the flow inside the cavity. All the other boundary walls are stationary throughout the simulation. From this, we can derive the boundary conditions for the velocity components as: $u = 0$, $v = -1$ at the moving boundary and $u = 0$, $v = 0$ at all the stationary boundaries. We set streamfunction values to be zero ($\psi = 0$) at all the boundaries. The Reynolds number for this flow is defined as $Re = \dfrac{v_0 R_0}{\nu}$, where v_0 is the magnitude of surface velocity of the side $\widehat{DA}$. This is imperative to mention here that all the boundary walls follow no-slip condition with the fluid inside the cavity, which supplies the following vorticity boundary conditions.

On the right wall AB, $\forall 1 \leq i \leq n_r$:

$$\omega_{i,1} = -\frac{2}{r_i^2 h_{\theta_1}^2}\psi_{i,2}. \tag{4.34}$$

On the top wall BC, $\forall 1 \leq j \leq n_\theta$:

$$\omega_{n_r,j} = -\frac{2}{h_{r_{n_r-1}}^2}\psi_{n_r-1,j}. \tag{4.35}$$

On the left wall CD, $\forall 1 \leq i \leq n_r$:

$$\omega_{i,n_\theta} = -\frac{2}{r_i^2 h_{\theta_{n_\theta-1}}^2}\psi_{i,n_\theta-1}. \tag{4.36}$$

On the bottom wall AB, $\forall 1 \leq j \leq n_\theta$:

$$\omega_{1,j} = -\frac{2}{h_{r_1}^2}\left(\psi_{2,j} - h_{r_1}\right) - \frac{1}{r_1}. \tag{4.37}$$

After we compute the values of vorticity, the boundary values for its gradients are calculated using one-sided approximations those are analogous to equations (3.8)–(3.11).

On the right wall AB, $\forall 1 \leq i \leq n_r$:

$$\phi_{\theta_{i,1}} = -\frac{h_{\theta_1}}{h_{\theta_2}(h_{\theta_1}+h_{\theta_2})}\phi_{i,3} + \frac{h_{\theta_1}+h_{\theta_2}}{h_{\theta_1}h_{\theta_2}}\phi_{i,2} - \frac{2h_{\theta_1}+h_{\theta_2}}{h_{\theta_1}(h_{\theta_1}+h_{\theta_2})}\phi_{i,1} + \mathcal{O}\left(h_{\theta_2}(h_{\theta_1}+h_{\theta_2})^2\right). \tag{4.38}$$

On the top wall BC, $\forall 1 \leq j \leq n_\theta$:

$$\begin{aligned}\phi_{r_{n_r,j}} =& \frac{h_{r_{n_r-1}}}{h_{r_{n_r-2}}(h_{r_{n_r-1}}+h_{r_{n_r-2}})}\phi_{n_r-2,j} - \frac{h_{r_{n_r-1}}+h_{r_{n_r-2}}}{h_{r_{n_r-1}}h_{r_{n_r-2}}}\phi_{n_r-1,j} \\ &+ \frac{2h_{r_{n_r-1}}+h_{r_{n_r-2}}}{h_{r_{n_r-1}}(h_{r_{n_r-1}}+h_{r_{n_r-2}})}\phi_{n_r,j} + \mathcal{O}\left(h_{r_{n_r-1}}(h_{r_{n_r-1}}+h_{r_{n_r-2}})^2\right).\end{aligned} \tag{4.39}$$

On the left wall CD, $\forall 1 \leq i \leq n_r$:

$$\begin{aligned}\phi_{\theta_{i,n_\theta}} =& \frac{h_{\theta_{n_\theta-1}}}{h_{\theta_{n_\theta-2}}(h_{\theta_{n_\theta-1}}+h_{\theta_{n_\theta-2}})}\phi_{i,n_\theta-2} - \frac{h_{\theta_{n_\theta-1}}+h_{\theta_{n_\theta-2}}}{h_{\theta_{n_\theta-1}}h_{\theta_{n_\theta-2}}}\phi_{i,n_\theta-1} \\ &+ \frac{2h_{\theta_{n_\theta-1}}+h_{\theta_{n_\theta-2}}}{h_{\theta_{n_\theta-1}}(h_{\theta_{n_\theta-1}}+h_{\theta_{n_\theta-2}})}\phi_{i,n_\theta} + \mathcal{O}\left(h_{\theta_{n_\theta-1}}(h_{\theta_{n_\theta-1}}+h_{\theta_{n_\theta-2}})^2\right).\end{aligned} \tag{4.40}$$

On the bottom wall DA, $\forall 1 \leq j \leq n_\theta$:

$$\phi_{r_{1,j}} = -\frac{h_{r_1}}{h_{r_2}(h_{r_1}+h_{r_2})}\phi_{3,j} + \frac{h_{r_1}+h_{r_2}}{h_{r_1}h_{r_2}}\phi_{2,j} - \frac{2h_{r_1}+h_{r_2}}{h_{r_1}(h_{r_1}+h_{r_2})}\phi_{1,j} + \mathcal{O}\left(h_{r_2}(h_{r_1}+h_{r_2})^2\right). \tag{4.41}$$

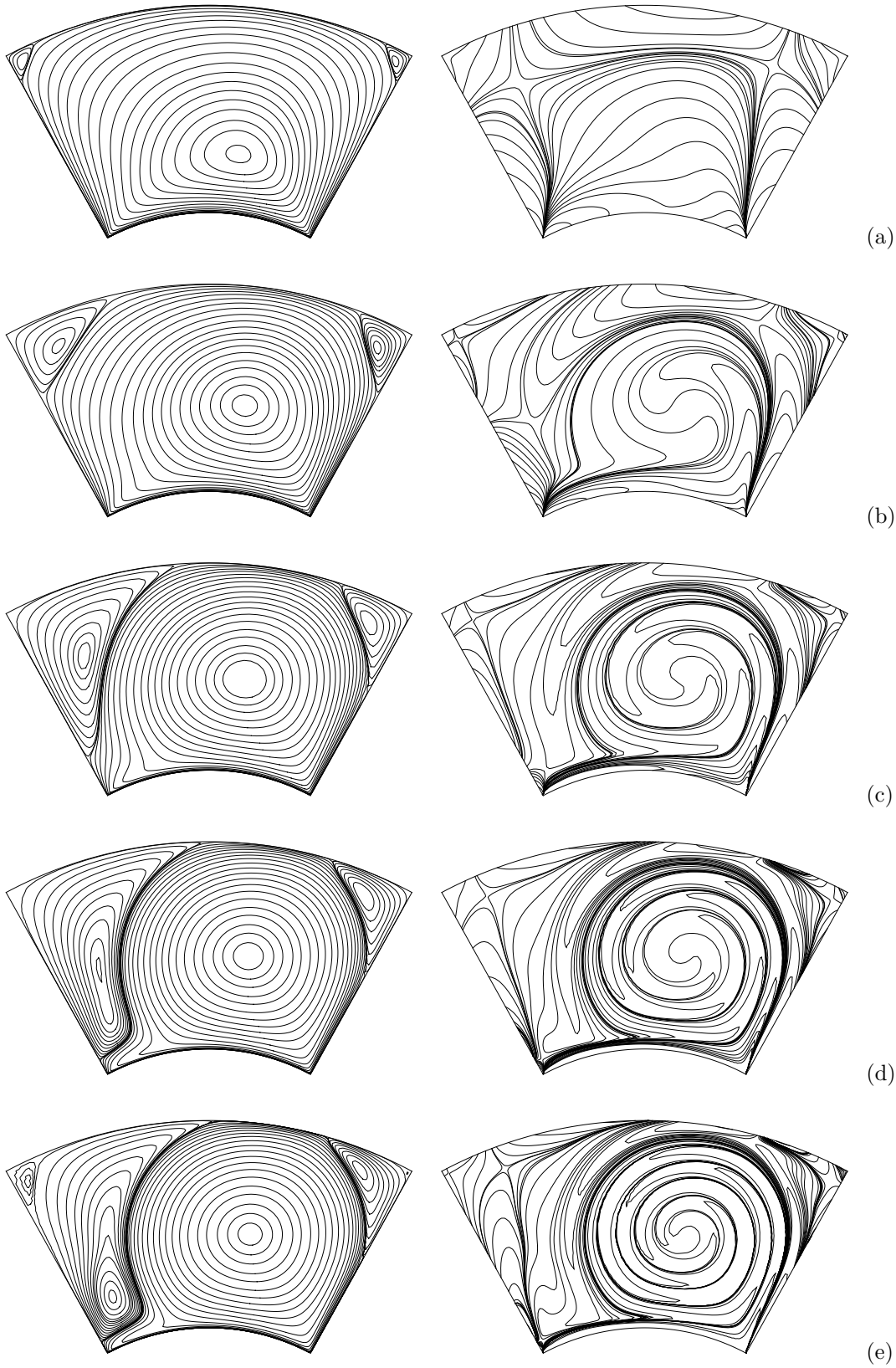

Fig. 4.5: Problem 3: Contours of streamfunction (left) and vorticity (right) computed with 65×65 grids: (a) $Re = 55$, (b) $Re = 350$, (c) $Re = 1000$, (d) $Re = 2000$, (e) $Re = 3000$.

While working with this problem, Lee and Tsuei [93] witnessed that large errors in the solution propagate near the rotating boundary. Besides, vortices are also created at the solid boundaries of the cavity. Therefore it is necessary to introduce maximum number of grids in the vicinity of cavity walls as can be seen in Fig. 4.4b. This has been achieved using modified versions of the grid generating equations (4.30) and (4.32) with proper choices of the constants $L_r = L_\theta = 1.0$, $\lambda_r = \lambda_\theta = -0.55$ and $\Theta_r = \Theta_\theta = 2\pi$.

The computations for this problem are carried out for Reynolds numbers 55, 350, 1000, 2000, 3000 and 5000. The post processed steady-state streamfunction (ψ) and vorticity (ω) contours for $55 \leq Re \leq 3000$ are plotted in Fig. 4.5. As Re increases, the primary vortex moves gradually towards the right wall of the cavity. Similar to the case of lid-driven square cavity, with increase in Reynolds number the secondary vortices opposite to the moving wall get bigger in size, particularly the secondary left vortex gains significantly more size as compared to the secondary right vortex and for higher values of Re the former tends to occupy the entire left side of the cavity. Further, at $Re = 3000$ a tertiary vortex is seen to form at the top left corner of the cavity. It is to be mentioned that all the findings are in accordance with those available in the literature [26, 93, 123, 132, 176] both experimentally and numerically. Furthermore, as the Re value increases, the vorticity contours shift from the cavity's center towards its walls, creating extremely strong vorticity gradients close to the walls.

Fig. 4.6 presents the velocity profiles along the radial line $\theta = \dfrac{\pi}{2}$ computed on grids of four different sizes 17×17, 33×33, 65×65 and 97×97 for $Re = 55$ and 350. We can see from these figures that the computed results are unaffected by the change in grid points and a 65×65 grid is sufficient to achieve grid-independent solution for both the Re values.

For this problem, we have also computed the perceived rate of convergence [30]. Despite best efforts, we could not trace the estimation of perceived order on nonuniform polar grid. The increased flow complexity in case of higher Re value makes the estimation of rate of convergence computation extensive [30]. Therefore,s the perceived order of convergence has been computed only for the cases $Re = 55$ and

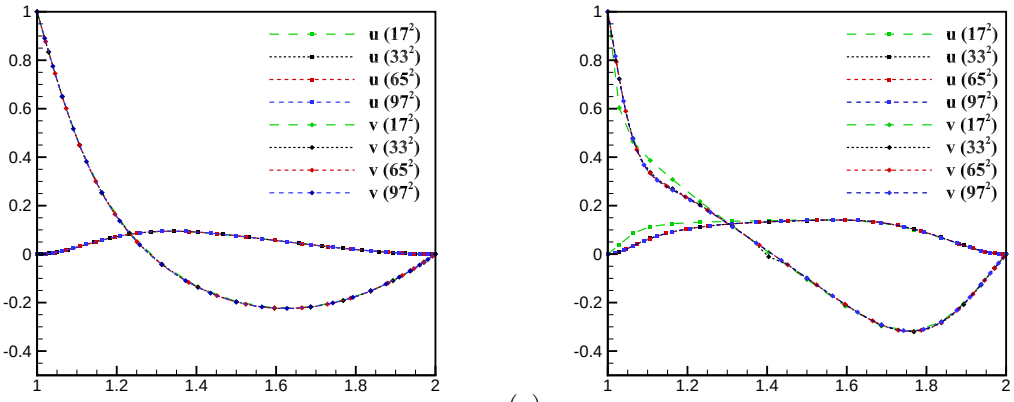

Fig. 4.6: Problem 3: The u and v velocities along the line $\theta = \dfrac{\pi}{2}$ computed on grids of different sizes: (a) $Re = 55$, (b) $Re = 350$.

350. We employ grids of three different sizes *viz.* 33×33, 65×65 and 97×97 and compute with $\delta t = 1.0e-4$ to minimize temporal error. The perceived order of convergence for streamfunction has been estimated in Table 4.7, whereas convergence of vorticity is compiled in Table 4.8. From these tables, we can observe that the order of convergence for vorticity in L_2-norm error drops below quadratic because of increased flow complexity. Moreover, it is amply clear that the mesh 97×97 should be ideally suited to compute in conjunction with the present discretization strategy.

Next, we carry out a qualitative comparison of the numerically attained results for $Re = 55$ and 350 with those of the experimental findings reported by Fuchs and Tillmark [45]. In Fig. 4.7 we present the numerically simulated streamlines for $Re = 55$ and 350 at the steady state along with those of the experimental ones. Moreover, the numerically obtained u and v velocities along $\theta = \dfrac{\pi}{2}$ are compared to those of [45] in Fig. 4.8. Both numerical and experimental solutions show good agreement with each other for each Re value. The u and v velocity profiles along the line $\theta = \dfrac{\pi}{2}$ for Re values 1000, 2000 and 3000 are presented in Fig. 4.9, though there is no quantitative evidence available for the same in the literature. Additionally, the distribution of the vorticity along $\widehat{DA}$ and $\theta = \dfrac{\pi}{2}$ are depicted in Fig. 4.10. It can be seen that both the radial and tangential velocities become stronger in the vicinity of the circular walls of the cavity, whereas the vorticity gradients can be seen to develop near all the boundary walls at higher values of Reynolds numbers. These

Table 4.7: Problem 3: L_1 and L_2-norm difference in streamfunction and perceived order of convergence in space.

Re	Grid size	L_1-norm	order	L_2-norm	order
55	33^2				
		$\|\psi_2 - \psi_1\|$=4.829202e-5		$\|\psi_2 - \psi_1\|$=7.723404e-5	
	65^2		3.17		2.64
		$\|\psi_3 - \psi_1\|$=6.470839e-5		$\|\psi_3 - \psi_1\|$=1.039171e-4	
	97^2				
350	33^2				
		$\|\psi_2 - \psi_1\|$=1.710546e-4		$\|\psi_2 - \psi_1\|$=2.594515e-4	
	65^2		2.61		2.41
		$\|\psi_3 - \psi_1\|$=2.469988e-4		$\|\psi_3 - \psi_1\|$=3.867575e-4	
	97^2				

Table 4.8: Problem 3: L_1 and L_2-norm difference in vorticity and perceived order of convergence in space.

Re	Grid size	L_1-norm	order	L_2-norm	order
55	33^2				
		$\|\omega_2 - \omega_1\|$=3.057162e-1		$\|\omega_2 - \omega_1\|$=2.983460e0	
	35^2		2.26		1.52
		$\|\omega_3 - \omega_1\|$=4.672710e-1		$\|\omega_3 - \omega_1\|$=5.259851e0	
	97^2				
350	33^2				
		$\|\omega_2 - \omega_1\|$=3.919087e-1		$\|\omega_2 - \omega_1\|$=3.232429e0	
	65^2		2.52		1.66
		$\|\omega_3 - \omega_1\|$=5.739092e-1		$\|\omega_3 - \omega_1\|$=5.534059e0	
	97^2				

observations are in line with those reported in [176]. In Tables 4.9 and 4.10, we have compiled all the quantitative data referring to the primary and secondary vortices. Tables 4.9 and 4.10 also carry out a comparison of strength and location of the

vortices with those available in the literature for $55 \leq Re \leq 3000$. It is heartening to notice that our computation compares well with the firmly established studies available in the literature.

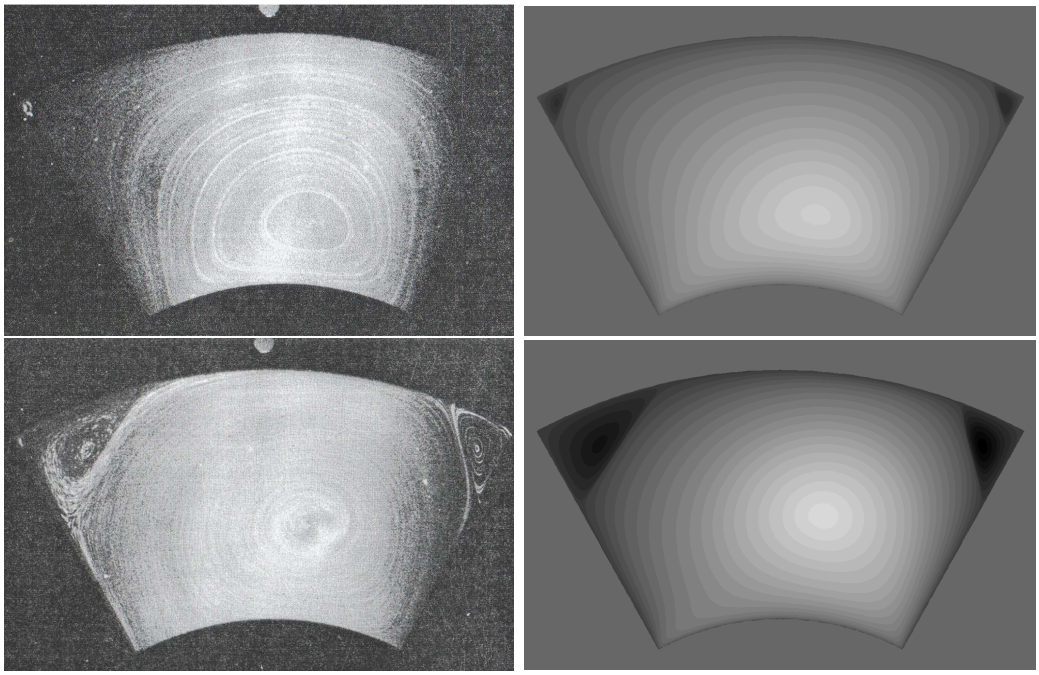

Fig. 4.7: Problem 3: Comparison of experimental [45] (left) and numerical (right) steady-state streamfunction contours of driven polar cavity problem: (a) $Re = 55$, (b) $Re = 350$.

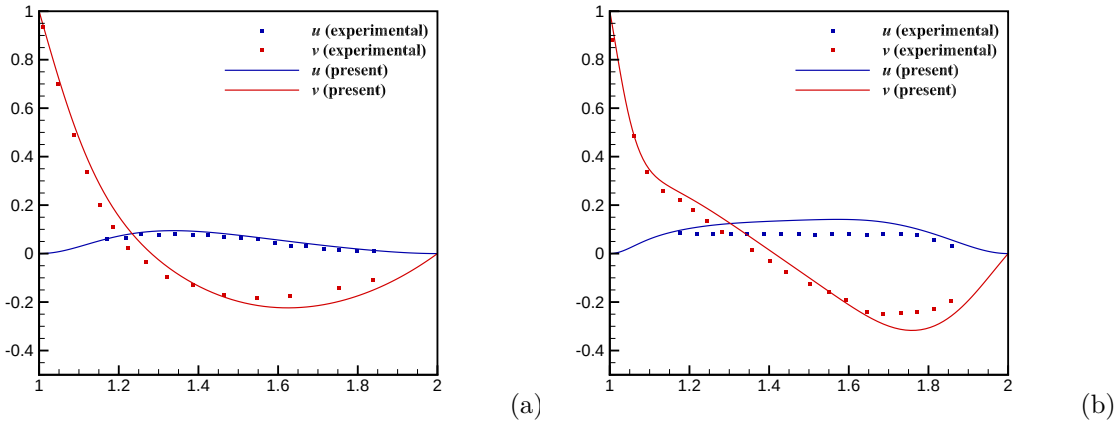

Fig. 4.8: Problem 3: Comparisons of steady-state u and v velocity profiles along the radial line $\theta = \dfrac{\pi}{2}$ with [45]: (a) $Re = 55$, (b) $Re = 350$.

Subsequently, we carry out our computation for $Re = 5000$ on a 129×129 nonuniform polar grid. To the best of our knowledge, the solution to this problem

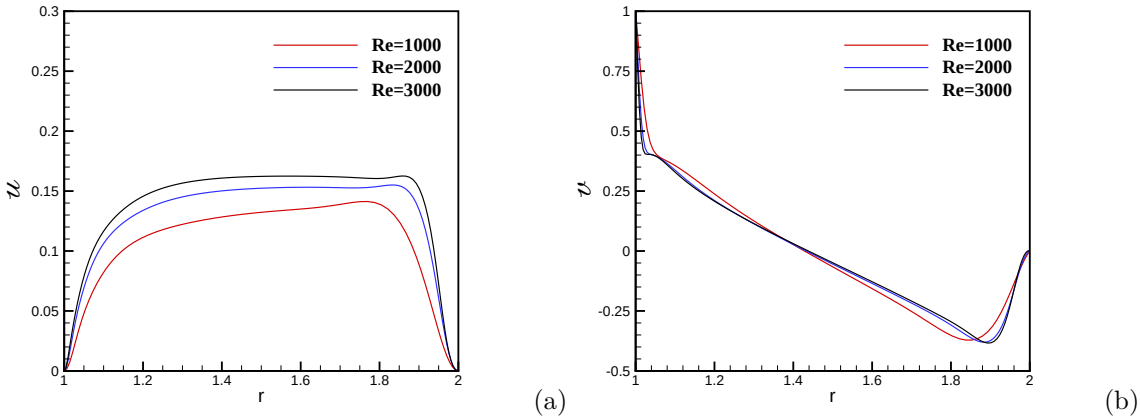

Fig. 4.9: Problem 3: Steady-state (a) u and (b) v velocity profiles along $\theta = \dfrac{\pi}{2}$ for different Re values.

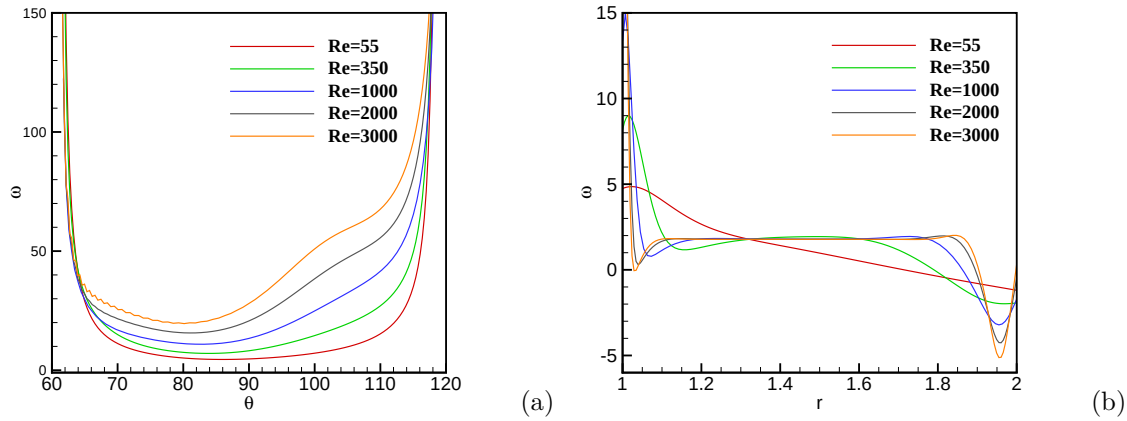

Fig. 4.10: Problem 3: Vorticity contours for different Re values along (a) the moving wall and (b) $\theta = \dfrac{\pi}{2}$.

for Reynolds numbers as high as 5000 has not been computed using a transient scheme. Sen and Kalita [132], in their work, used a steady code to arrive at a converged solution at $Re = 5000$. Also, authors used a 83×119 grid with exponential clustering at the inner wall along the radial direction. In this work, we intend to better capture the physics of the flow and hence use appropriate clustering near all boundaries. It is interesting to notice that the present discretization of the N-S equations shows a gradual convergence towards a stable periodic solution rather than a steady-state solution as reported in [132]. Time evolution of the physical property of the flow inside the cavity helps to establish the periodic nature of the solution.

Table 4.9: Problem 3: Strength and position of the centre of primary vortex for different Reynolds numbers.

Re		Grid Size	ψ_{max}	x	y
55	[176]	513×513	0.1155	0.141	1.281
	[132]	83×119	0.1155	0.138	1.285
	[26]	81×81	0.1156	0.142	1.285
	Present	65×65	0.1153	0.143	1.282
350	[176]	513×513	0.1263	0.167	1.414
	[132]	83×119	0.1263	0.163	1.411
	[26]	81×81	0.1266	0.171	1.414
	Present	65×65	0.1243	0.158	1.411
1000	[176]	513×513	0.1275	0.169	1.439
	[132]	83×119	0.1275	0.166	1.436
	[26]	81×81	0.1275	0.174	1.444
	Present	65×65	0.1270	0.167	1.448
2000	[176]	513×513	0.1253	0.188	1.447
	Present	97×97	0.1250	0.194	1.447
3000	[132]	109×157	0.1240	0.196	1.447
	Present	97×97	0.1237	0.194	1.447

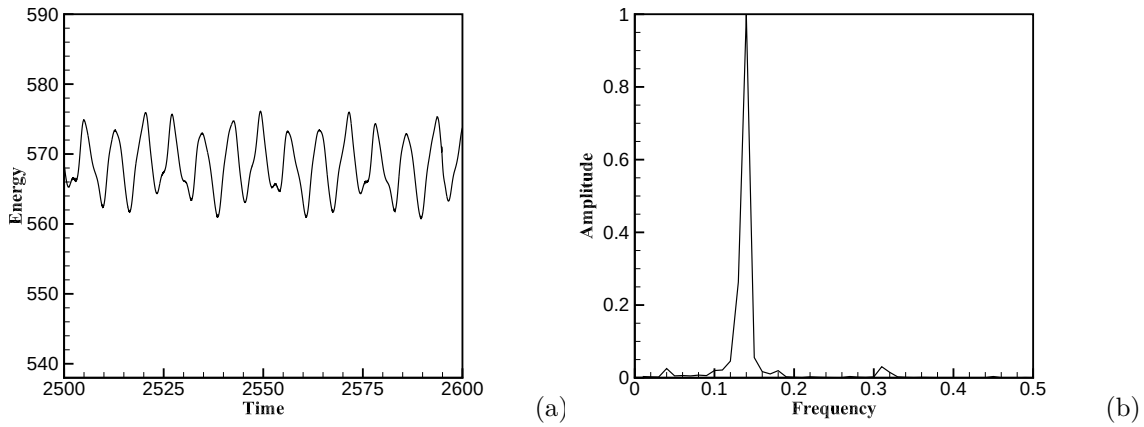

Fig. 4.11: Problem 3: (a) Temporal progression and (b) power spectrum of total energy of the flow inside a polar cavity for $Re = 5000$.

Table 4.10: Problem 3: Strength and position of the centre of secondary vortices for different Reynolds numbers.

		Secondary Right			Secondary Left		
Re		ψ_{min}	x	y	ψ_{min}	x	y
55	[176]	-8.690e-6	0.881	1.730	-4.690e-6	-0.880	1.729
	[132]	-7.964e-6	0.883	1.731	-4.994e-6	-0.876	1.742
	[26]	-8.102e-6	0.882	1.735	-4.391e-6	-0.882	1.735
	Present	-9.602e-6	0.879	1.726	-5.140e-6	-0.879	1.726
350	[176]	-5.490e-4	0.794	1.697	-3.990e-4	-0.702	1.695
	[132]	-5.469e-4	0.796	1.690	-4.009e-4	-0.696	1.699
	[26]	-5.435e-4	0.796	1.689	-4.010e-4	-0.701	1.703
	present	-5.525e-4	0.790	1.692	-3.388e-4	-0.704	1.697
1000	[176]	-2.120e-3	0.757	1.713	-3.460e-3	-0.590	1.552
	[132]	-2.099e-3	0.755	1.717	-3.480e-3	-0.589	1.549
	[26]	-2.106e-3	0.762	1.705	-3.488e-3	-0.592	1.559
	Present	-2.238e-3	0.749	1.729	-3.446e-3	-0.599	1.537
2000	[176]	-3.080e-3	0.734	1.743	-4.830e-3	-0.522	1.406
	Present	-3.151e-3	0.734	1.734	-4.835e-3	-0.519	1.393
3000	[132]	-3.325e-3	0.724	1.757	-7.089e-3	-0.459	1.156
	Present	-3.559e-3	0.714	1.770	-7.062e-3	-0.452	1.149

Temporal progression of the total energy inside the cavity is presented in Fig. 4.11a. We perform the spectral density analysis for the variation of energy which results in a single frequency peak as can be seen in Fig. 4.11b. This further ascertains the periodicity of the flow. Nevertheless, accurate estimation of the frequency and time-period of the solution leaves further scope of investigation of this problem.

4.4.4 Problem 4: Natural convection in horizontal concentric annulus

We further analyze the efficiency of the newly developed scheme to tackle heat transfer by implementing it to solve natural heat convection inside a horizontal

concentric annulus. This problem has gained a considerable amount of attention from researchers over the years because of its relevance and applicability in various engineering and physical situations, such as heat exchangers, solar collectors, nuclear reactors, thermal energy storage systems, etc. [25, 85, 102, 121, 137, 140, 162, 174, 184]. It is governed by the transient Boussinesq equations which in the polar coordinate system are given as

$$\begin{cases} \omega_t = Pr\left(\omega_{rr} + \dfrac{1}{r}\omega_r + \dfrac{1}{r^2}\omega_{\theta\theta}\right) - \left(u\omega_r + \dfrac{v}{r}\omega_\theta\right) \\ \qquad\qquad + RaPr\left(\mathscr{T}_r\cos\theta - \mathscr{T}_\theta\dfrac{\sin\theta}{r}\right), & (4.42a) \\ \omega = -\left(\psi_{rr} + \dfrac{1}{r}\psi_r + \dfrac{1}{r^2}\psi_{\theta\theta}\right), & (4.42b) \\ \mathscr{T}_t = \left(\mathscr{T}_{rr} + \dfrac{1}{r}\mathscr{T}_r + \dfrac{1}{r^2}\mathscr{T}_{\theta\theta}\right) - \left(u\mathscr{T}_r + \dfrac{v}{r}\mathscr{T}_\theta\right). & (4.42c) \end{cases}$$

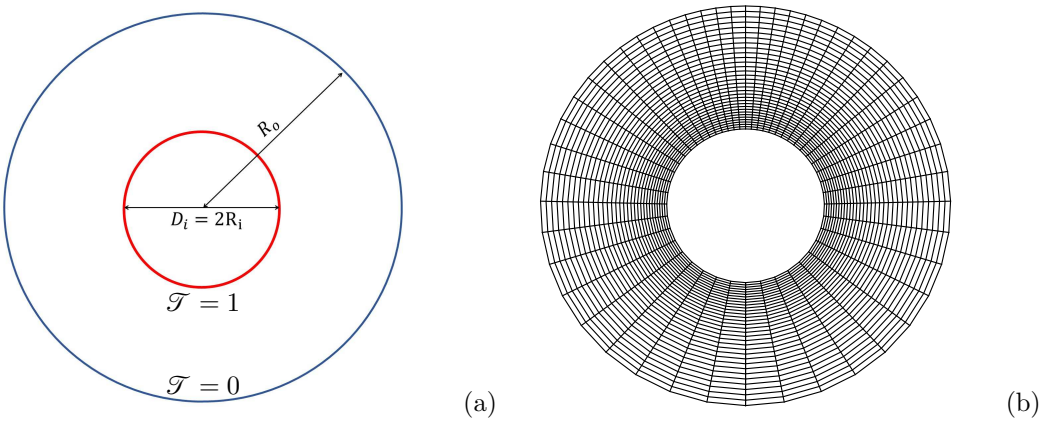

Fig. 4.12: Problem 4: (a) Problem setup and (b) typical noununiiform polar grid for heat transfer in horizontal annulus.

The problem setup consists of two concentric circular walls of which the inner circle has a radius R_i and the outer circle has a radius R_o. Two different temperatures are maintained at the circular walls of the annulus as shown in Fig. 4.12a. The simulation is carried out for Ra values 2.38×10^3, 9.50×10^3, 4.70×10^4, 6.19×10^4 and 1.02×10^5. The values of the Pr is set as 0.706, 0.717 and 0.718. For each case, we have considered $L/D_i = 0.8$, where $L = R_o - R_i$ and $D_i = 2R_i$. The inner wall is heated to a unit nondimensional temperature ($\mathscr{T} = 1$) keeping the outer wall's temperature at zero ($\mathscr{T} = 0$). This temperature difference serves as the driving

force for the flow in this simulation. The values of streamfunction and vorticity at the inner and outer boundaries of the annulus are obtained respectively from no-slip criteria between the fluid and the walls of the annulus and one-sided approximations introduced in equations (4.38)–(4.41). The prior studies help us to identify that the near boundary region of the inner circle and the radial line $\theta = \frac{\pi}{2}$ should be observed cautiously. This motivates us to work with a mesh where grid points are clustered in these regions (see Fig. 4.12b). The grid is generated by making adequate changes in equations (4.30) and (4.32) and choosing the associated parameters as $L_r = 0.8$, $L_\theta = 2\pi$, $\Theta_r = \pi$, $\Theta_\theta = 2\pi$, $\lambda_r = -0.4$ and $\lambda_\theta = 0.25$.

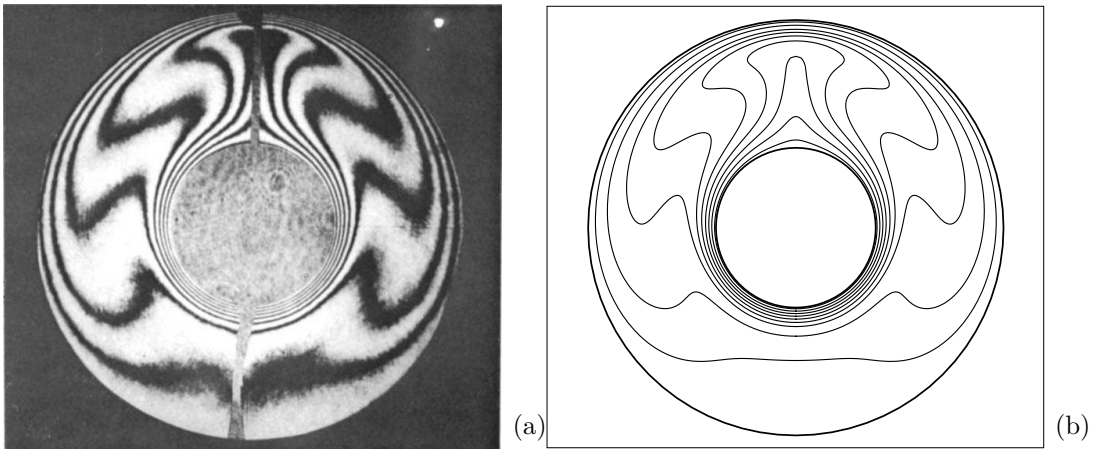

Fig. 4.13: Problem 4: Steady-state isotherms at $Ra = 4.7 \times 10^4$, $Pr = 0.706$: (a) experimental solution [85] and (b) numerical solution.

The numerical results obtained from the present simulation have been presented in Fig. 4.13 and 4.14. We carry out a qualitative comparison in Fig. 4.13 where the numerically obtained steady-state isotherm contours for $Ra = 4.7 \times 10^4$, $Pr = 0.706$ are depicted alongside that of the experimental study [85]. The figure illustrates how the fluid near the cold outer wall of the annuli flows down to the bottom due to buoyancy caused by the temperature difference, while the fluid near the hot inner wall of the annulus flows up along the inner boundary and a strong plume emerges above the inner boundary at $\theta = \frac{\pi}{2}$. The temperature field symmetry occurs as the flow achieves a steady state. Good agreements are obtained between the experimental and numerical solutions. Fig. 4.14 contains the steady-state isotherms alongside the streamfunctions for different Ra values. The figure shows that for lower

Ra values natural convection is dominated by heat conduction. Almost concentric isotherms can be seen for $Ra = 2.38 \times 10^3$ while two symmetric vortices can be seen caused by the weak natural convection. As the value of Ra increases the fluid motion driven by buoyancy force also increases, leading to a stronger convection. Accordingly, the isotherms start moving upward and change shape to form a plume. The plume becomes more prominent with a further increase in the Ra value.

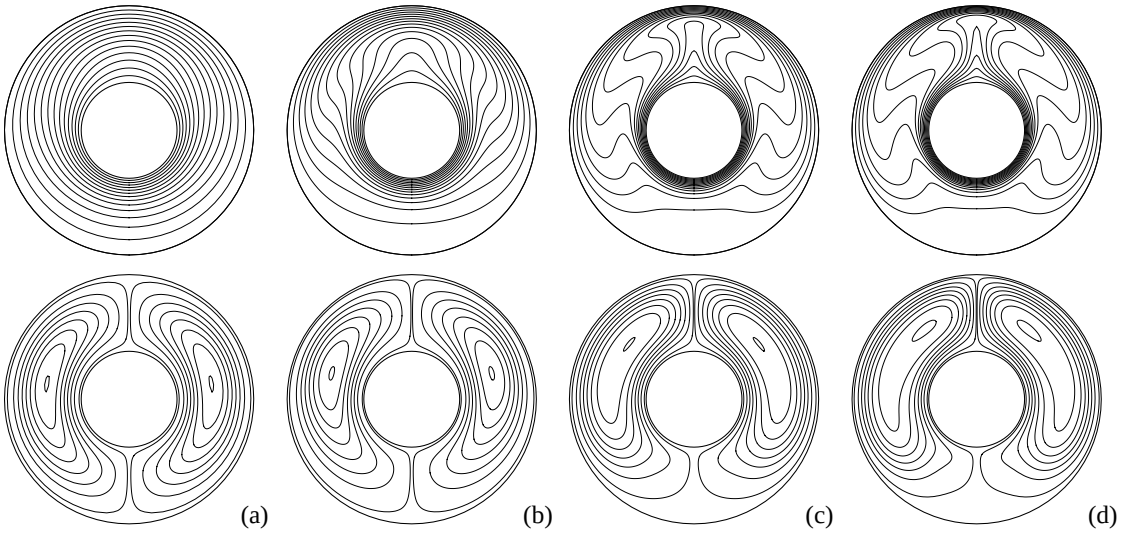

Fig. 4.14: Problem 4: Steady-state isotherms and streamlines: (a) $Ra = 2.38 \times 10^3$, (b) $Ra = 9.50 \times 10^4$, (c) $Ra = 6.19 \times 10^4$, (d) $Ra = 1.02 \times 10^5$.

Additionally, for this problem we have also evaluated the average Nusselt number ($\overline{Nu}$), which is the arithmetic mean of the surface-averaged Nusselt numbers of the annulus walls that are defined as

$$Nu^i = -\frac{1}{\pi} R_i \int_{-\frac{\pi}{2}}^{\frac{\pi}{2}} \mathscr{T}_r|_{r=R_i} \, d\theta \tag{4.43}$$

and

$$Nu^o = -\frac{1}{\pi} R_o \int_{-\frac{\pi}{2}}^{\frac{\pi}{2}} \mathscr{T}_r|_{r=R_o} \, d\theta. \tag{4.44}$$

The average Nusselt number thus obtained is compared to the existing studies in Table 4.11. Our computed values agree well with those available in the literature at $Ra = 2.38 \times 10^3$, Pr=0.716. But it is seen to differ by about 10% as Ra is increased.

Table 4.11: Problem 4: Comparison of average nusselt number ($\overline{Nu}$) computed using different schemes for different Rayleigh numbers.

Ra	Pr	[85](expt.)	[137]	[140]	Present
2.38×10^3	0.716	1.38		1.320	1.3882
9.50×10^3	0.717	2.01	1.9901	1.999	1.6909
6.19×10^4	0.718	3.32	3.3092	3.361	2.9176
1.02×10^5	0.718	3.66	3.6475	3.531	3.2994

4.4.5 Problem 5: Forced convection over a stationary heated circular cylinder

Finally, we carry out numerical simulation for the classical problem of heat transfer in the fluid flow over the stationary heated circular cylinder. The stationary heated circular cylinder is presumed to be of unit radius ($R_0 = 1$) and immersed in a fluid of infinite domain maintained at unit nondimensional temperature [7, 17, 34, 58, 69, 87, 90, 110, 127, 132, 145, 147, 171]. The cylinder is kept in a cross-flow having uniform velocity $u = U_\infty = 1$. The 2D flow configuration of the problem is shown in Fig. 4.15. The cylinder is placed at the center of the circular domain. Following [43], we have set the far-field boundary at a distance $R_\infty = 45R_0$. On the solid surface $r = R_0$, the velocity components follow the no-slip boundary conditions, i.e. $u = v = 0$ and hence $\psi = 0$. At the far stream $r = R_\infty$ in front of the cylinder, the potential flow is prescribed a unit value $u = U_\infty = 1$. For this problem, where the simulation results in periodic vortex shedding, we have imposed the convective boundary conditions $\phi_t + U_\infty \phi_r = 0$ (where ϕ represents ψ, u or v) at the downstream boundary, to capture the shedding process efficiently. In the direction of the flow, the convective boundary conditions can best facilitate continuous shedding of vortices when they leave the computational domain [12, 72, 91, 167]. In addition, at the far field vorticity value decays and becomes $\omega = 0$. However, it possesses nonzero value at the inner boundary, which may be derived by making use of the fact that $\psi = 0$, $\psi_r = 0$ on $r = R_0$ in equation (4.42b). The vorticity gradients at all the boundaries are computed using one-sided approximations.

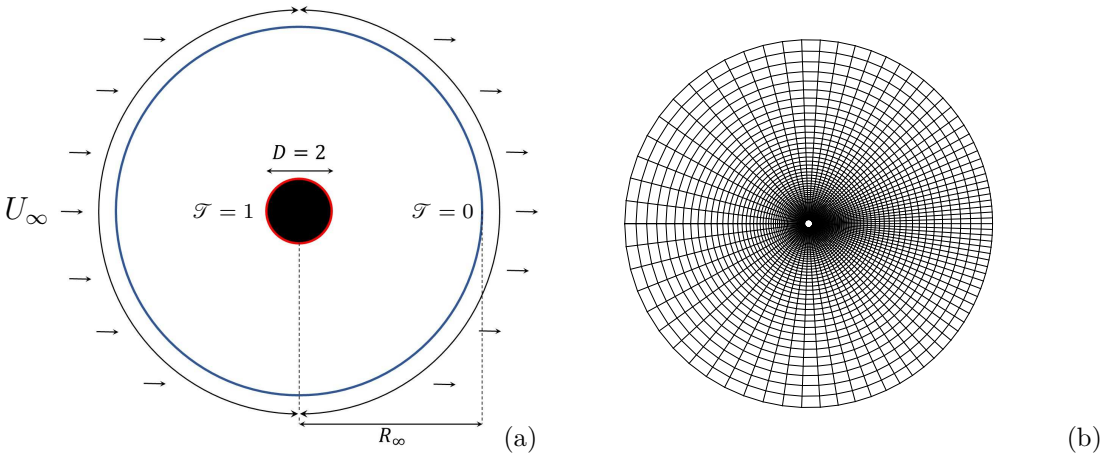

Fig. 4.15: Problem 4: (a) Configuration of the problem and (b) typical 65×97 nonuniform grid.

The Reynolds number (Re) and the Prandtl number (Pr) are the essential nondimensional parameters for this problem. In this present investigation, we fix the Prandtl number at $Pr = 0.7$ for all the values of Re under consideration. As shown in Fig. 4.15, the computational domain is discretized using a nonuniform grid of size 129×193 for all the combinations of Pr and Re. With the circular cylinder placed at the center of the domain, grid is clustered around the cylinder wall.

In this problem, we calculate the drag (C_D) and lift coefficients (C_L) using the following formulas [69, 84, 143],

$$C_D = \frac{1}{Re} \int_0^{2\pi} \left\{ \left(\frac{\partial \omega}{\partial r} \right)_{R_0} - \omega_{R_0} \right\} \sin\theta d\theta, \tag{4.45}$$

$$C_L = \frac{1}{Re} \int_0^{2\pi} \left\{ \left(\frac{\partial \omega}{\partial r} \right)_{R_0} - \omega_{R_0} \right\} \cos\theta d\theta. \tag{4.46}$$

We start by verifying the grid-independence of the present numerical solution. Here, we compute for $Re = 10$ and present the distribution of surface vorticity and local Nusselt number (Nu^0) for three grids of different sizes *viz.* 65×97, 97×129 and 129×193 in Fig. 4.16. Here, angle θ is measured in the counterclockwise direction starting from the rear stagnation point of the cylinder. The figures show that the numerical results are nonresponsive to the change in grid points and a grid of size 129×193 is sufficient for accurate simulation of the flow.

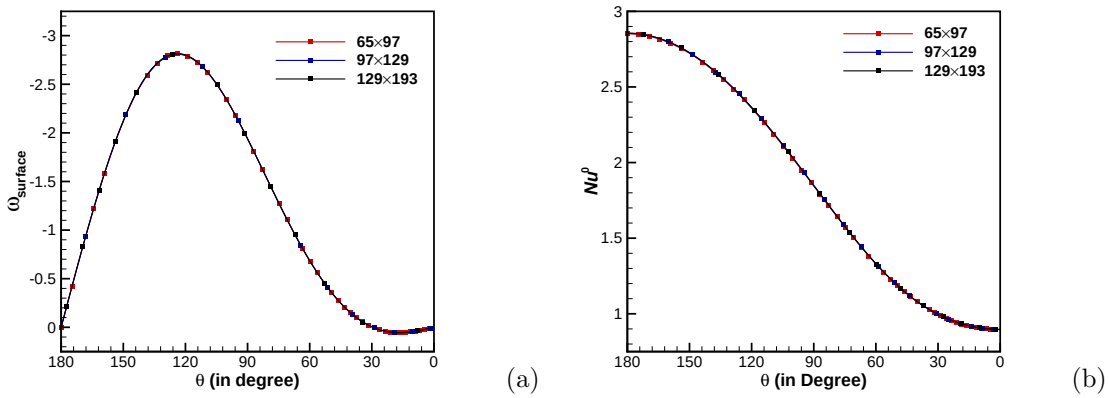

Fig. 4.16: Problem 4: Distribution of (a) vortcity and (b) local Nusselt number at steady state along the cylinder surface for $Re = 10$.

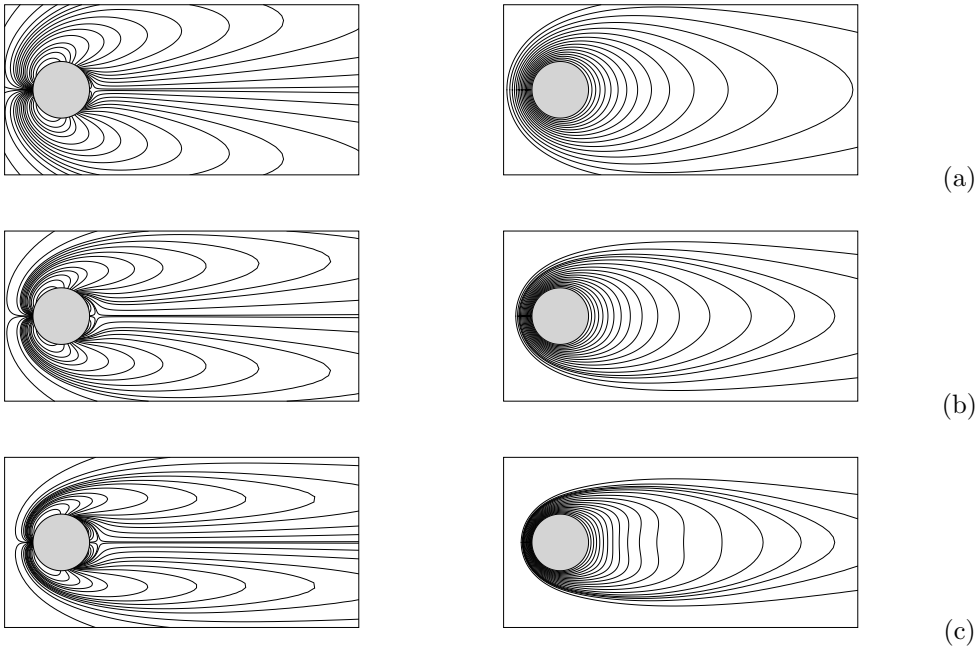

Fig. 4.17: Problem 4: Steady-state vorticity contours (left) and isotherms (right): (a) $Re = 10$, (b) $Re = 20$, (c) $Re = 40$.

A validation study is first performed for low Reynolds number flows. At the low Reynolds number range ($Re \leq 50$), the vortex structure in the wake remains steady and symmetric, thus the temperature field shows similar steady and symmetric characteristics as well. Here, we select to work with $Re = 10$, 20, 40 and 45. Fig. 4.17 depicts the symmetric vorticity and isotherm contours at steady state for various Reynolds numbers. Similar vorticity and isotherm patterns can be found in

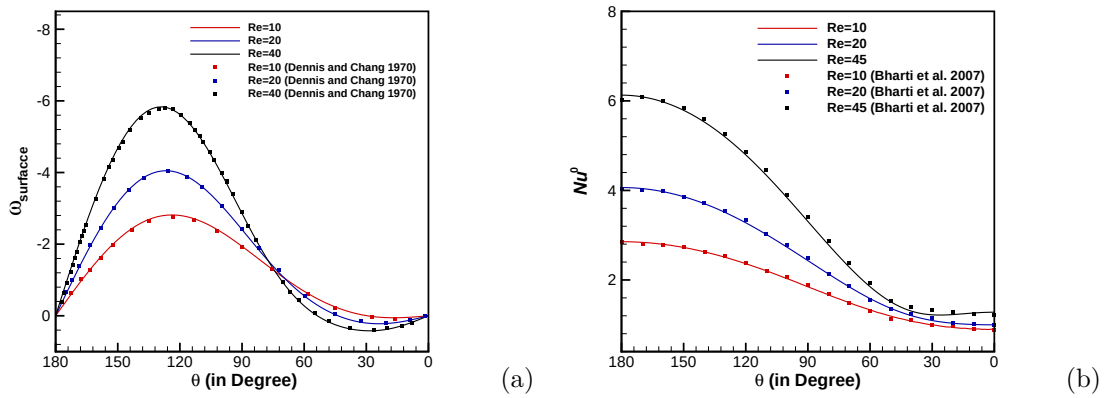

Fig. 4.18: Problem 4: Comparison of (a) surface vorticity distribution for $Re = 10$, 20 and 40 and (b) local Nusselt number distribution for $Re = 10$, 20 and 45 with existing numerical results [7, 31].

various studies available in the literature.

Present results of surface distribution of vorticity for $Re = 10$, 20 and 40 and local Nusselt number for $Re = 10$, 20 and 45 are portrayed in Fig. 4.18a and 4.18b respectively; these values are compared with the previous numerical results from Dennis and Chang [31] and Bharti *et al.* [7]. It can be seen that the two sets of data show excellent agreement with each other. The largest value of the local Nusselt number is obtained at the front stagnation point of the cylinder; the value of the Nusselt number then reduces gradually towards the rear stagnation point and attains its lowest value thereat (see Fig. 4.18b). In Table 4.12, we have compiled our computed values of L/D, where L is the length of the recirculation bubble formed behind the cylinder, the drag coefficient C_D and the average Nusselt number $\overline{Nu}$ for $Re = 10$, 20 and 40. As can be seen from the figures and table, the recirculation length and the average Nusselt number depend directly on Re, while the drag coefficient varies inversely. Table 4.12 presents a quantitative comparison of the present solution. Computational results are compared with reference data [7, 17, 34, 58, 69, 87, 90, 110, 127, 132, 145, 147, 171]. Once again, the adaptability of the present scheme is evident from the proximity of our results with the results reported in prior well-established studies.

Next, we are interested in studying the flow for $Re = 100$, 140 and 200. The

Table 4.12: Problem 4: Comparison of steady-state wake length, drag coefficient and average Nusselt number for different Re.

		$Re = 10$	%-diff.	$Re = 20$	%-diff.	$Re = 40$	%-diff.
L/D	[58]	0.237	4.22	0.921	0.54	2.245	0.36
	[110]			0.945	3.07	2.26	0.31
	[127]			0.885	3.50	2.105	7.03
	[171]			0.93	1.51	2.31	2.47
	[69]			0.917	0.11	2.207	2.08
	[132]	0.252	1.98	0.926	1.08	2.323	3.01
	[17]			0.95	3.58	2.39	5.73
	[87]	0.266	7.14	0.937	2.24	2.139	5.33
	Present	0.247		0.916		2.253	
C_D	[58]	3.170	10.50	2.152	4.23	1.499	2.33
	[110]			2.144	3.68	1.589	3.46
	[127]			2.0597	0.06	1.5308	0.21
	[171]			2.091	1.43	1.565	1.98
	[69]			2.0193	2.07	1.5145	1.29
	[132]	2.699	5.11	1.949	5.75	1.439	6.60
	[17]			2.119	2.74	1.582	3.03
	[87]	2.690	5.46	2.160	4.58	1.576	2.66
	Present	2.837		2.061		1.534	
$\overline{Nu}$	[34]	1.8673	0.37	2.5216	2.32	3.4317	4.48
	[90]	1.8101	2.57	2.4087	2.26	3.2805	0.08
	[147]	1.6026	15.86	2.2051	11.70	3.0821	6.35
	[145]	1.8600	0.18	2.4300	1.36	3.2000	2.43
	[7]	1.8623	0.30	2.4653	0.09	3.2825	0.14
	[17]	1.8671	0.56	2.4718	0.35	3.2912	0.41
	Present	1.8567		2.4631		3.2778	

transition of the vorticity and isotherm contours from steady to periodic state for Re=100 is depicted in Fig. 4.19. This may be considered as the representation of the flow for the other Re values considered, although each requires a different time to attain periodicity. As can be seen in Fig. 4.19a, there is no formation of a vortex

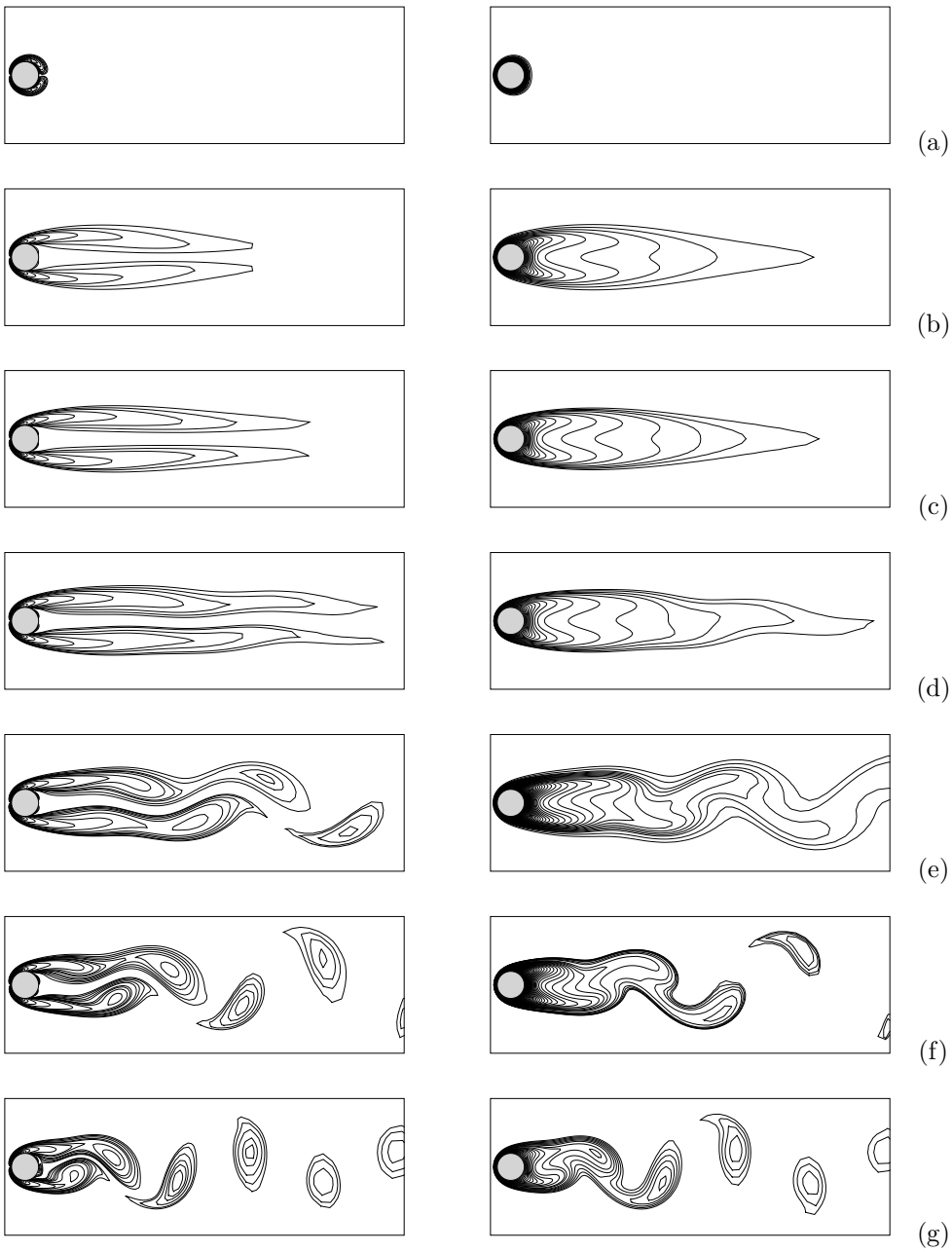

Fig. 4.19: Problem 4: Evolution of vorticity (left) and isotherms (right) for $Re = 100$ at (a) $t = 0.5$, (b) $t = 25$, (c) $t = 50$, (d) $t = 75$, (e) $t = 90$, (f) $t = 100$, (g) $t = 250$.

structure in the flow field initially. Nevertheless, at the beginning, a thermal boundary layer is seen to be generated near the surface of the heated cylinder. As time marches, two opposite symmetrical vortices are formed simultaneously which grow in size with time, and remain symmetrically stable for a particular period as shown in Fig. 4.19b and 4.19c. During this period, the thickness of the thermal boundary layer increases; the temperature distribution also remains symmetric about the

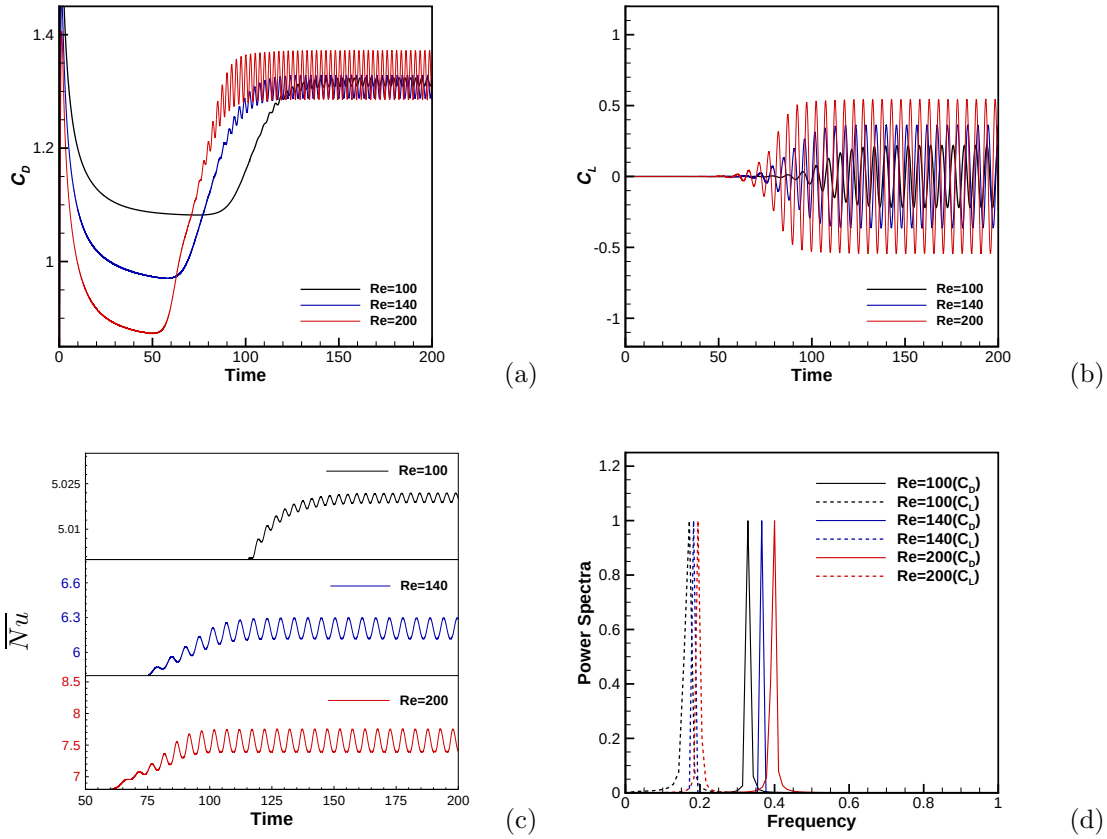

Fig. 4.20: Problem 4: Temporal evolution of (a) C_D, (b) C_L, (c) ($\overline{Nu}$) at the cylinder surface, (d) power spectra of C_D and C_L for $Re = 100$, 140 and 200.

line $\theta = 0$. After a certain point of time, a fluctuation develops in the flow which destroys the symmetry in the vortices and temperature distribution and they start to oscillate downstream which can be noticed in Fig. 4.19d. As the flow develops further, the length and breadth of vortices at the rear of the cylinder continue to grow and eventually are shed from the cylinder towards downstream while heat is transported. It is heartening to see that the present scheme could capture the characteristic feature of the periodic flow, the so-called von Kármán vortex street very efficiently. With the vortex shedding taking place, confined hot fluid clusters are observed in the flow (see Fig. 4.19e). Subsequently, Fig. 4.19f and 4.19g indicate the synchronized variation of flow and temperature fields, where vortex shedding phenomena plays a decisive role in the heat transfer at the downstream.

The time history of the drag coefficient (C_D), lift coefficient (C_L) and aver-

age Nusselt number ($\overline{Nu}$) displayed in Fig. 4.20a–4.20c pertinently implies that the newly developed scheme has accurately captured the periodic state for all the Reynolds numbers considered for the study. The periodicity is further justified by the single dominating peak for C_D and C_L in the spectral density analysis (see Fig. 4.20d). The distribution of local Nusselt number (Nu^0) over the cylinder surface for different Re values are represented in Fig. 4.21a. In Fig. 4.21b we carry out a qualitative comparison between the surface distribution of Nu^0 for $Re = 200$ computed in the present study with those of [109, 183]; which reveals close agreement of the present results with those taken from the literature. We then compare the numerical values of the flow parameters C_D, C_L, St and $\overline{Nu}$ with existing studies in Table 4.13. The numerical streaklines for $Re = 140$ computed using the present scheme is presented in Fig. 4.22, along with the streakline reported in the experimental work of Taneda [153]. From the comparison we note that vortex creation and dissipation as captured in the experimental work is effectively computed by the current formulation. Exceptional similarity between the present numerical results and the existing numerical and experimental results indeed verify and validate the scheme.

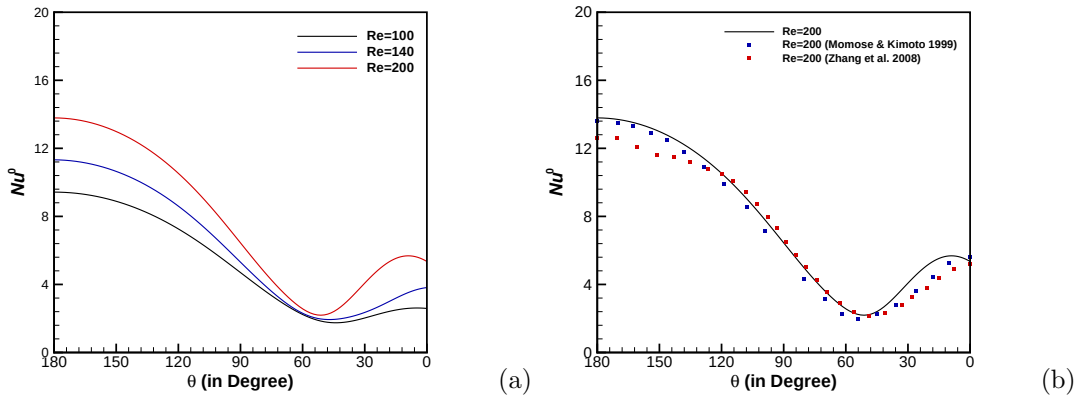

Fig. 4.21: Problem 4: (a) Distribution of local Nusselt number on the cylinder surface for $Re = 100$, 140, 200 and (b) comparison of local Nusselt number distribution over the cylinder surface for $Re = 200$ with results from [109, 183].

Table 4.13: Problem 4: Comparison flow parameters C_D, C_L, St and $\overline{Nu}$ for different Re.

		$Re = 100$	$Re = 140$	$Re = 200$
C_D	[92]	1.37 ± 0.009		1.34 ± 0.030
	[6]	1.38 ± 0.010		1.37 ± 0.046
	[129]	1.394 ± 0.007		1.357 ± 0.038
	[86]	1.325 ± 0.026		1.333 ± 0.046
	Present	1.317 ± 0.008	1.308 ± 0.020	1.329 ± 0.043
C_L	[92]	± 0.323		± 0.430
	[6]	± 0.340		± 0.700
	[129]	± 0.191		± 0.453
	[86]	± 0.306		± 0.351
	Present	± 0.22	± 0.361	± 0.543
St	[92]	0.160		0.187
	[6]	0.169		0.200
	[129]	0.165		0.197
	[86]	0.162		0.200
	Present	0.172	0.183	0.195
$\overline{Nu}$	[19]	5.12	5.87	7.15
	[18]	5.26		7.67
	[183]			7.23
	[15]	5.07	6.08	
	Present	5.02	6.20	7.55

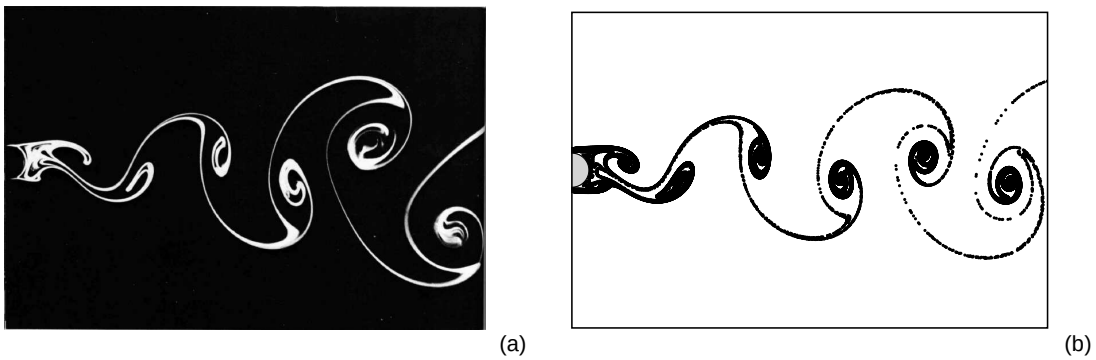

Fig. 4.22: Problem 4: Comparison between the instantaneous streaklines for $Re = 140$ captured in the (a) experimental study of Taneda [153] and (b) present computation.

4.5 Conclusion

In this chapter, we extend the philosophy of previous chapter for 2D transient convection and diffusion equation on Cartesian coordinates to polar coordinates to tackle nonrectangular geometries. The transformation-free HOC finite difference scheme proposed here can be applied directly on polar grids, unlike most of the schemes from the literature on polar grids which use transformation between physical and computational domain. We have also combined the virtue of nonuniformity with the present scheme. This levitates the efficiency and robustness of the scheme as it acquires the advantage of accumulating and scattering grid points as necessary. The formulation has theoretical accuracy of order two in both space and time. Subsequently, a novel HOC scheme with third-order spatial convergence and second-order temporal convergence has also been developed in this chapter. Extensive comparison revealed negligible difference in numerical solutions computed using these two methods. It is worthwhile to mention that for linear problems with analytical solution both the schemes exhibit a spatial convergence of order four which is higher than the theoretical values. Although, the third-order accurate scheme bears the same efficiency as the second-order accurate scheme, it turned out to be more expensive in regard to computational time. This encouraged us to employ the second-order accurate scheme on the rest of the test problems. The robustness of this scheme is examined by applying it to as many as three benchmark problems of fluid flow and heat flow, *viz.* driven polar cavity, natural convection in horizontal concentric annulus and forced convection around a heated stationary cylinder. In order to resolve the Neumann type boundary conditions, we have also introduced one-sided approximation for first-order derivatives. For the problem of forced convection around heated stationary cylinder, both the steady and periodic solutions are being accurately captured by the present scheme. Additionally, important aspects such as the von Kármán vortex phenomena and influence of vortex shedding on the heat transfer are also studied comprehensively for this fluid body interaction problem. The accuracy of the computed solutions is estimated from the results obtained in the test problems, which are very close to the existing results both qual-

itatively and quantitatively. We have reported the perceived order of convergence for all the variables in flow problems which are not supplemented with analytical solutions. It is heartening to see that our solutions could attain the theoretical order of convergence both spatially and temporarily in all the cases.